EXTENDED OPERATIONAL RANGE OF A FEEDBACK-CONTROLLED OPTICAL MICROPHONE FOR AEROACOUSTICS RESEARCH

By

Sara Feeney

A THESIS

Submitted to
Michigan State University
in partial fulfillment of the requirements
for the degree of

MASTER OF SCIENCE

Mechanical Engineering

2012

ABSTRACT

EXTENDED OPERATIONAL RANGE OF A FEEDBACK-CONTROLLED OPTICAL MICROPHONE FOR AEROACOUSTICS RESEARCH

By

Sara Feeney

This study is an extension of a previous study conducted at MSU on a feedback-controlled optical microphone for potential use in "beam-forming" arrays employing anywhere from thirty to one hundred microphones in aeroacoustics research. The membrane of the microphone is made from PVDF (polyvinylidene-fluoride), a material with piezoelectric properties, giving a means for opposing the sound-produced deflection of the membrane using a feedback loop. The feedback capability of the microphone allows it to self-calibrate and gives it response-matching capabilities in array applications—a unique advantage over current microphone technology, as manual, individual calibration of each microphone in an array can be time-consuming.

The present research goal is to extend the operational range of the microphone. Two provisions were proposed to accomplish this goal: the addition of a microphone back-plate with small holes to create a means to damp the membrane motion; also, by employing an optical sensor that measures membrane displacement averaged over an area rather than at a point, as used in the previous study, to attenuate the high-order resonance modes which cause instability in the control. The improved feedback microphone will ultimately enhance the capability of "beam-forming" arrays used for research. The results show that individually, each of the damping and area-averaged sensing was able to improve the operational range of the microphone, and together, they combined for an even greater improvement in stability, leading to tripling of the bandwidth of the baseline open-loop microphone.

TABLE OF CONTENTS

LIST OF TABLES

LIST OF FIGURES

Chapter 1

Introduction

Modern aeroacoustics measurements rely on the use of a large number of microphones in "beam-forming" arrays. Such arrays are used systematically by NASA, as well as other agencies and industry, to characterize, and hence utlimately mitigate acoustic noise emanating from aircraft during takeoff and landing [1]. Typically, a beam-forming array employs anywhere from thirty to one hundred microphones that must have a known calibration and matched phase response. The basic operating principle of the array involves using slight differences in the phase of the measured waveforms by the microphones in the beam-forming array to calculate the location of the acoustic point source.

Various microphones are currently used in beam-forming arrays, including instrument grade condenser microphones and electret microphones. Condenser microphones' operating principle is that the stretched metallic microphone membrane and a conductive back-plate situated a small distance behind it act as the two plates of a capacitor. Acoustic pressure causes the diaphragm to deflect, leading to change in the capacitance with the membrane motion. In a DC-biased condenser microphone, an approximately fixed charge is applied to the plates and the voltage across the plates changes with the capacitance change. Commercial condenser microphones are available which are individually calibrated and have a high degree of phase uniformity within ±10° at 10 kHz [1]. At a cost of approximately \$2000 per channel, typical arrays (containing 30 or more microphones) using this microphone technology can be very expensive. Furthermore, the calibration of the array microphones before tests is essential for accurate measurements. Given the large number of microhpones in an array, the calibration is time-consuming. Moreover, if the array is used for measurement in the field, the laboratory-determined calibration may be altered by environmental factors.

An inexpensive option is to use the electret microphone. An electret is a material with an embedded electric charge. In an electret microphone, the electret is attached to the backplate. Operation is similar to a condenser microphone without the need for a high-voltage power supply. While this lowers the cost, electret microphones are known to vary widely with respect to mechanical and electrical sensitivity and phase. Moreover, their response tends to drift due to environmental effects, and the polarized electret material loses its charge over time.

An alternative to the above microphone technologies is the concept of a feedback-controlled microphone. In this technology, membrane motion is detected and nullified using some means, for example an opposing pressure produced electrostatically or electromagnetically, through a feedback control loop integrated into the sensor. A feedback-controlled microphone has been developed recently at MSU. A proof of concept study of this new microphone type was successfully undertaken [2], [3]. The feedback provision of the microphone allows it to "self-calibrate" and gives it response-matching capabilities—a unique advantage over current

---

[1] Datasheet - Brüel & Kjær Type 4958 20kHz Precision Array Microphone

microphone technology which results in considerable time and cost savings for aeroacoustics tests. Previously existing feedback-controlled microphones are summarized in [3]. The microphone described in [2] is unique in that the combination of actuation and sensing techniques is being used for the first time and data exists to demonstrate the advantages of the feedback-controlled microphone, whereas other studies lacked such evidence.

The focus of the present thesis is to improve the design and extend the operational range of the feedback-controlled microphone developed in [2]. The baseline design as well as the proposed improvements are outlined in the following chapters. Specifically, perforated backplates were fabricated and incorporated into the microphone design as a means of mechanical damping of the membrane motion. The microphone response was then characterized to show the damping of all membrane resonance modes. Secondly, the previous design utilized a fiber-optic lever displacement sensor that averages displacement over a small point located at the center of the membrane. By employing a commercially available sensor that averages displacement over a larger area, the observability of higher-order membrane resonance modes decreases relative to the fundamental resonance mode. The increase in operational range was examined through the frequency response for this microphone design. The microphone was also characterized with the two above provisions implemented simultaneously.

Chapter 2

Methods and Modeling

2.1 Microphone Components

2.1.1 PVDF Film Microphone Capsule

The capsule design of the microphone prototype is shown in Figure 2.1. A 28μm PVDF (polyvinelidine-fluoride) film constitutes the diaphragm. The piezoelectric property of the membrane provides the actuation means for the feedback. The membrane is clamped between two aluminum pieces—the capsule body and the clamping ring, fabricated on a lathe from a piece of stock. The lip around the center hole puts tension in the membrane. And the rubber gasket between the pieces provides a seal; it also insulates the aluminum pieces from each other as they act as electrical conductors to the two metallized sides of the PVDF film. The screws attaching the two aluminum pieces are nylon so as to be nonconducting. On the opposite end of the microphone, a second rubber gasket between the capsule body and the acrylic plate further seals the cavity behind the membrane for the purposes of pressurization; the capsule is internally pressurized to improve electrical actuation sensitivity (in membrane deflection per unit voltage), as will be seen in section 2.4.1. Pressurization is fulfilled through connecting a pressurized air source to the pressure tap in the acrylic back-plate.

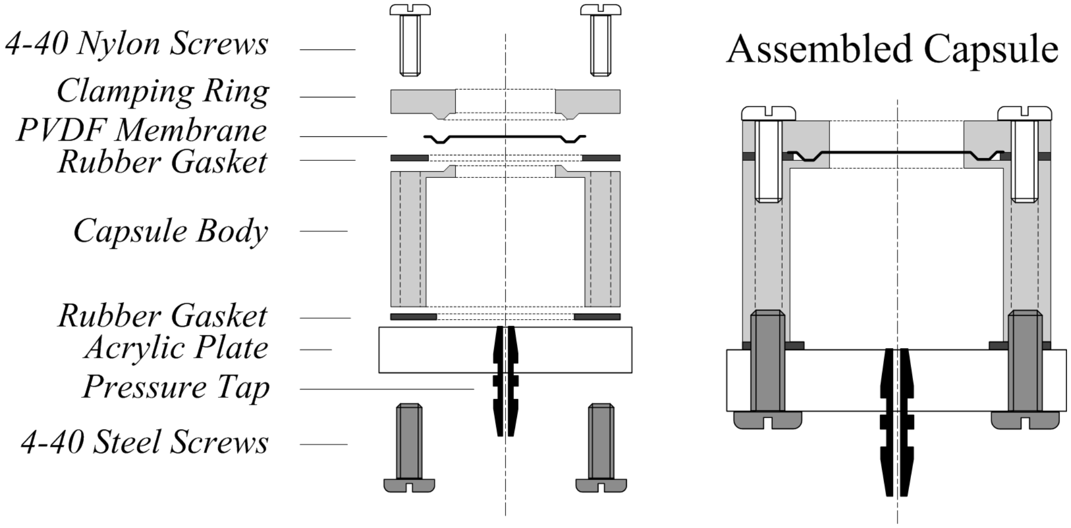

Figure 2.1: Exploded view (left) and assembled view (right) of the microphone capsule

2.1.2 Pressurization System

Figure 2.2 shows the schematic of the pressurization system used to induce curvature on the PVDF membrane. It is a well-established fact that curvature of the membrane will result in an increase of actuation sensitivity [4], [5], [6]. Air is directed from a high pressure air system in the building into the microphone back chamber through the pressure tap. Pressurization level is manually controlled by a series of valves and monitored with a pressure transducer. The integrated pressure sensor is model MPX4010DP and it has 0.45 V/kPa sensitivity with a 0.14V offset for input up to 10kPa. A one-gallon tank is connected to the pressurization line to reduce any line pressure fluctuations.

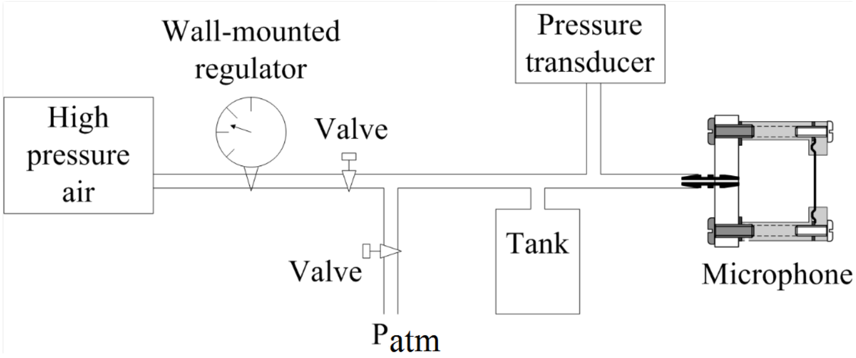

Figure 2.2: Schematic diagram of the system used to pressurize the microphone cavity

2.1.3 Fiber-Optic Lever Displacement Sensor

The displacement of the PVDF diaphragm in response to incident acoustic pressure is sensed using a fiber-optic lever displacement sensor. The baseline design utilizes a Philtec model D20 optical sensor, which measures deflection at virtually a point (0.51mm tip diameter) at the center of the membrane. Figure 2.3 shows a schematic of the fiber-optic sensor.

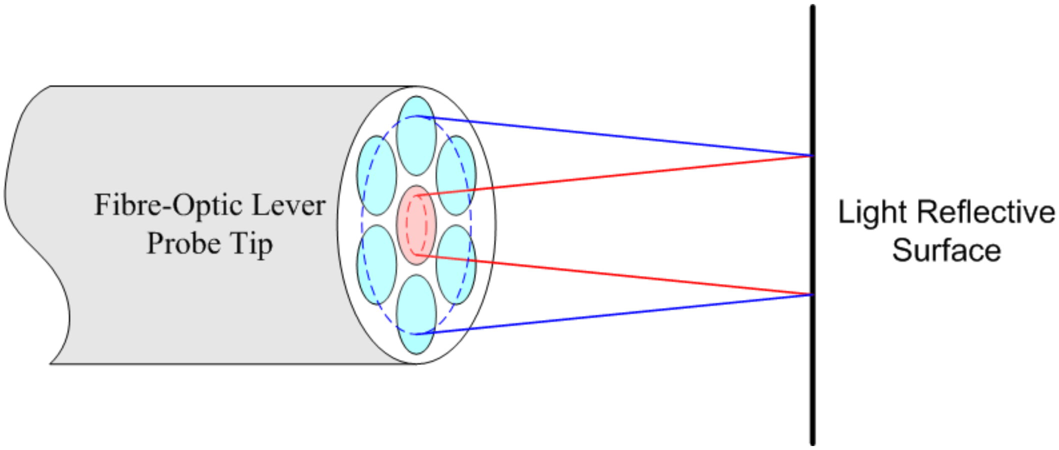

Figure 2.3: Schematic drawing of fiber-optic lever probe; red and blue lines indicate incident and reflected light respectively; for interpretation of the references to color in this and all other figures, the reader is referred to the electronic version of this thesis.

Light is emitted from the transmitting fiber and reflected off the membrane surface back to receiving fibers. A photodetector detects the intensity of the reflected light. The corresponding voltage-to-displacement relation is such that the voltage first increases with distance between the membrane and sensor tip before reaching a peak and then beginning to decrease. A typical voltage-to-displacement relation is shown in Figure 2.4. As seen from the figure, the sensor's response has two relatively linear portions in the "near-" and "far-side" operating ranges. For accurate calibration, the peak voltage is always set to five volts before a microphone characterization is carried out. This adjustment may be necessary due to fluctuations in temperature or humidity in the room. Because the fiber-optic lever sensor is more sensitive in the "near-side" range, the operating point is set in the middle of this range.

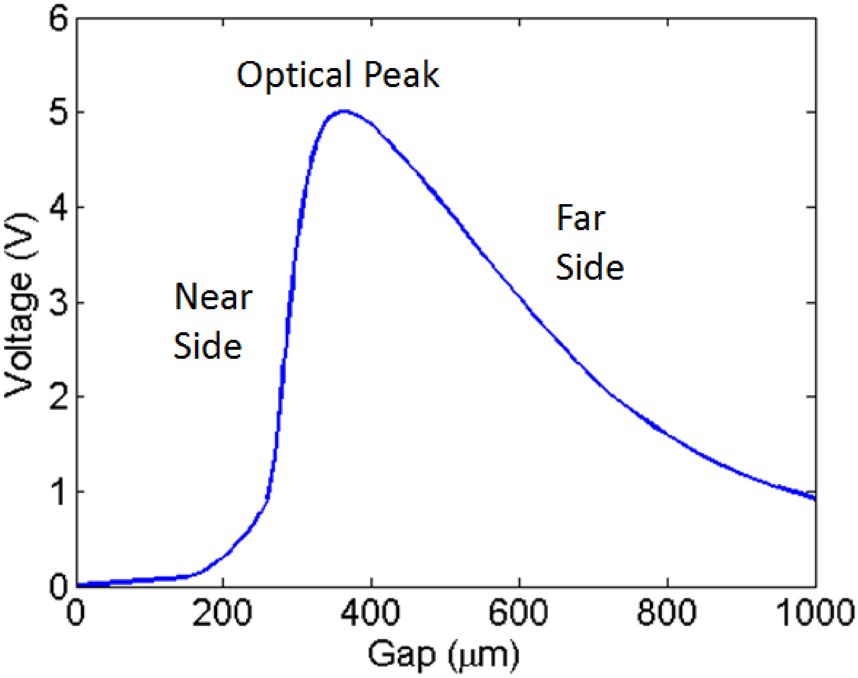

Figure 2.4: Typical Philtec fiber-optic sensor response

Chapter 4 describes results obtained using an area-averaging optical sensor, Philtec model D169, with a tip diameter of 4.29mm. As will be explained in Chapter 4, in utilizing the area-averaging sensor, the sensed membrane deflection due to high-order resonance modes is attenuated by spatial averaging of those modes relative to that produced by the fundamental resonance. This type of attenuation is one of the two mechanisms explored in this study as ways of increasing the range of controller gains/sensor response over which stable sensor operation is maintained.

The optical sensor transfer function is given in equation (2.1) and is based on a manufacturer given cut-off frequency of 20kHz and a first-order dynamical system model.

$$G_O(s) = \frac{79400}{\frac{s}{125600} + 1}(V/m) \tag{2.1}$$

2.1.4 Piezo Driver

Figure 2.5 shows a block diagram of the microphone in feedback operation. The piezoelectric system represents the piezoelectric driving circuit employed to drive the PVDF membrane in response to the output of the lever sensor. For these experiments, a ThorLabs model MDT691 is used; it provides a gain of 15 and a maximum output between 0 and 150V. During operation, a DC offset of 75V is imposed using a knob on the front panel of MDT691. This centers the PVDF driving voltage in the middle of the operating range, enabling attainment of membrane driving voltage swings of up to the full 150V range, peak to peak. The transfer function of the peizo driver is taken simply as a flat magnitude with no phase delay. This decision is based on the insignificant value of the phase of the piezo driver relative to the amount of phase delay caused by the dynamic response of the fiber-optic sensor.

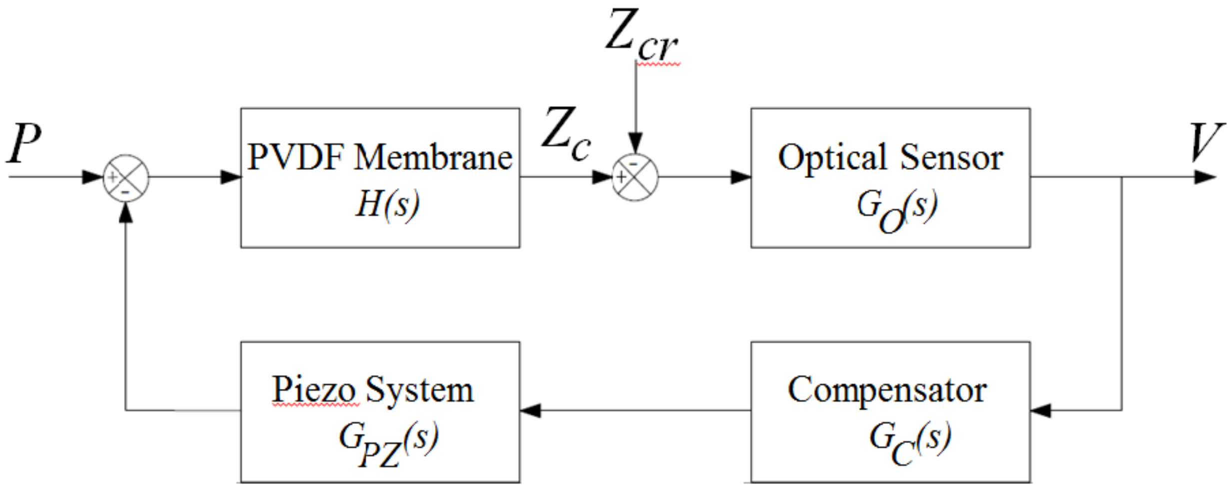

Figure 2.5: Block diagram of the microphone in closed-loop operation. Note that P, Z_c, Z_{cr}, and V are the Laplace transforms of the acoustic pressure, actual and reference central membrane deflection, and output voltage respectively.

2.1.5 Feedback Controller

For the feedback control, a new compensator was built modeled after the one used in [3]. The phase-lead compensator (see compensator in Figure 2.5) has three user-specified parameters to achieve the desired transfer function: proportional gain K_p, derivative gain K_d, and corner frequency f_c. Varying these parameters allow the *effective* membrane's mass (M), stiffness (K), and damping (C) to be altered. This enables tuning of the frequency response of the microphone, and hence, in a beam-forming array, several capsules can be phase matched (a crucial characteristic for the accuracy of beam-forming measurements).

Figure 2.6 shows a schematic of the operational-amplifier-based circuit for the compensator. Terminology for the components for the rebuilt controller are kept consistent with their counterparts in previous research [3]. Resistors are represented by R_{p1}, R_{p2}, R_{d2}, and $R_{f,sum}$, while digital potentiometers R_p, R_d, and R_c control proportional gain, derivative gain, and corner frequency. A LabVIEW program called "DigitalControllerNew.vi" is used to set the digital potentiometers. A fixed capacitance is represented by C. The rationale for creating a new controller was to have the ability to swap out capacitances for the case when higher derivative gains (K_d) were needed. The new controller was built on a breadboard, thus giving ease in switching out components.

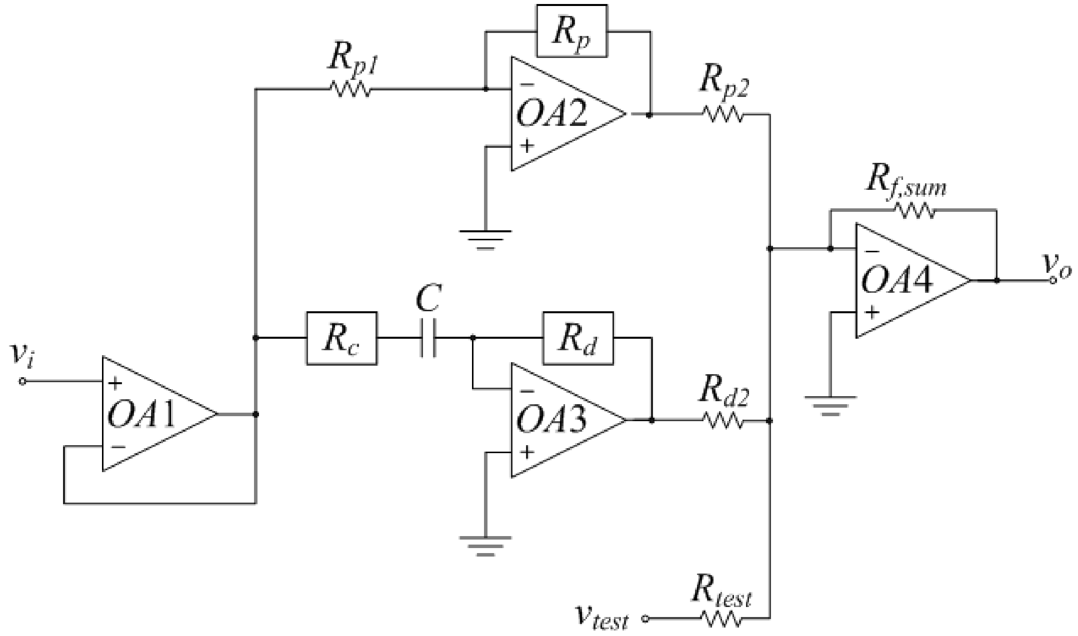

Figure 2.6: Circuit schematic for the phase-lead compensator

The transfer function for the controller $G_C(s)$ is given in equation (2.2)

$$G_C(s) = K_p + \frac{K_d s}{\tau_d s + 1} \tag{2.2a}$$

$$K_p = \frac{R_p R_{f,sum}}{R_{p1} R_{p2}} \tag{2.2b}$$

$$K_d = \frac{R_d R_{f,sum} C}{R_{d2}} \tag{2.2c}$$

$$fc = \frac{1}{2\pi R_c C} \tag{2.2d}$$

The resistance and capacitance values employed are listed in Table 2.1. The corresponding minimum and maximum K_p, K_d, and f_c values are listed in Table 2.2.

Table 2.1: Electrical components used in the phase-lead compensator depicted in Figure 2.6

Symbol	Type	Value
$OA1$	Op-amp	UA741CN
$OA2$	Op-amp	UA741CN
$OA3$	Op-amp	UA741CN
$OA4$	Op-amp	UA741CN
R_{p1}	Resistor	1.794 kΩ
R_{p2}	Resistor	2.202 kΩ
R_{d2}	Resistor	2.208 kΩ
$R_{f,sum}$	Resistor	21.96 kΩ
R_{test}	Resistor	22.04 kΩ
R_p	Digital Pot	MCP42050
R_d	Digital Pot	MCP42100
R_c	Digital Pot	MCP42010
C	Capacitor	0.022 μF

Table 2.2: Minimum and maximum values for the user-defined controller variables

	K_p	$K_d(s)$	$f_c(Hz)$
minimum	0.36	1.61E-5	1500
maximum	143	9.59E-3	222000

Before using the new compensator, it had to be calibrated to verify its operation. To do so, a sinusoidal voltage sweep from 0 to 25kHz was connected to the compensator input, voltage v_i (Figure 2.6), using an HP model 33120A function generator. The resulting output voltage (v_o) as well as v_i were recorded digitally in order to obtain the magnitude and phase response of the compensator. The data acquisition and processing details employed are similar to those used for acoustic and electrical calibration of the microphone, which are described in detail in section 2.2.

Figure 2.7 shows some calibration plots for a low K_p value, while Figure 2.8 shows some calibration plots for a high K_p value within the available range (see Table 2.2). All results are obtained for $f_c = 6000$, and a low, intermediate, and high value of K_d. Figures 2.7 and 2.8 show that except for an early high frequency roll-off, the actual and expected controller responses are consistent. The early roll-off is believed to be due to the limitation of the gain-bandwidth product of operational amplifiers in the circuit. Attempts to remedy this issue were made by using some higher bandwidth op-amps. However, these chips were electrostatic sensitive and prone to noise in the signal. Recommendations for future work are to employ thin film resistors and special capacitors in conjunction with the higher bandwidth op-amps in the circuit.

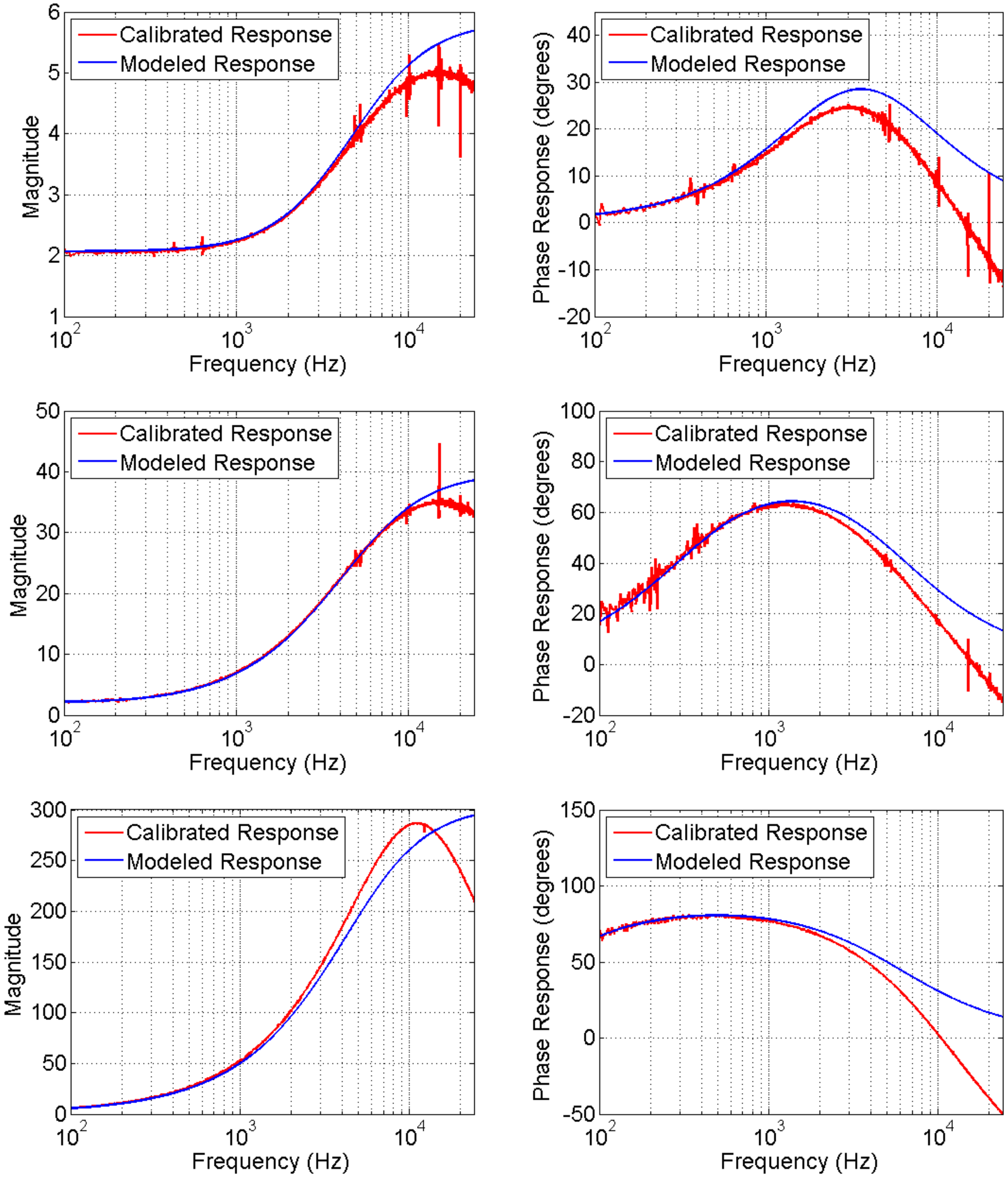

Figure 2.7: Controller calibration for low proportional gain $K_p = 2$ and $f_c = 6000$; $K_d = 0.0001$ (top); $K_d = 0.001$ (center); $K_d = 0.008$ (bottom)

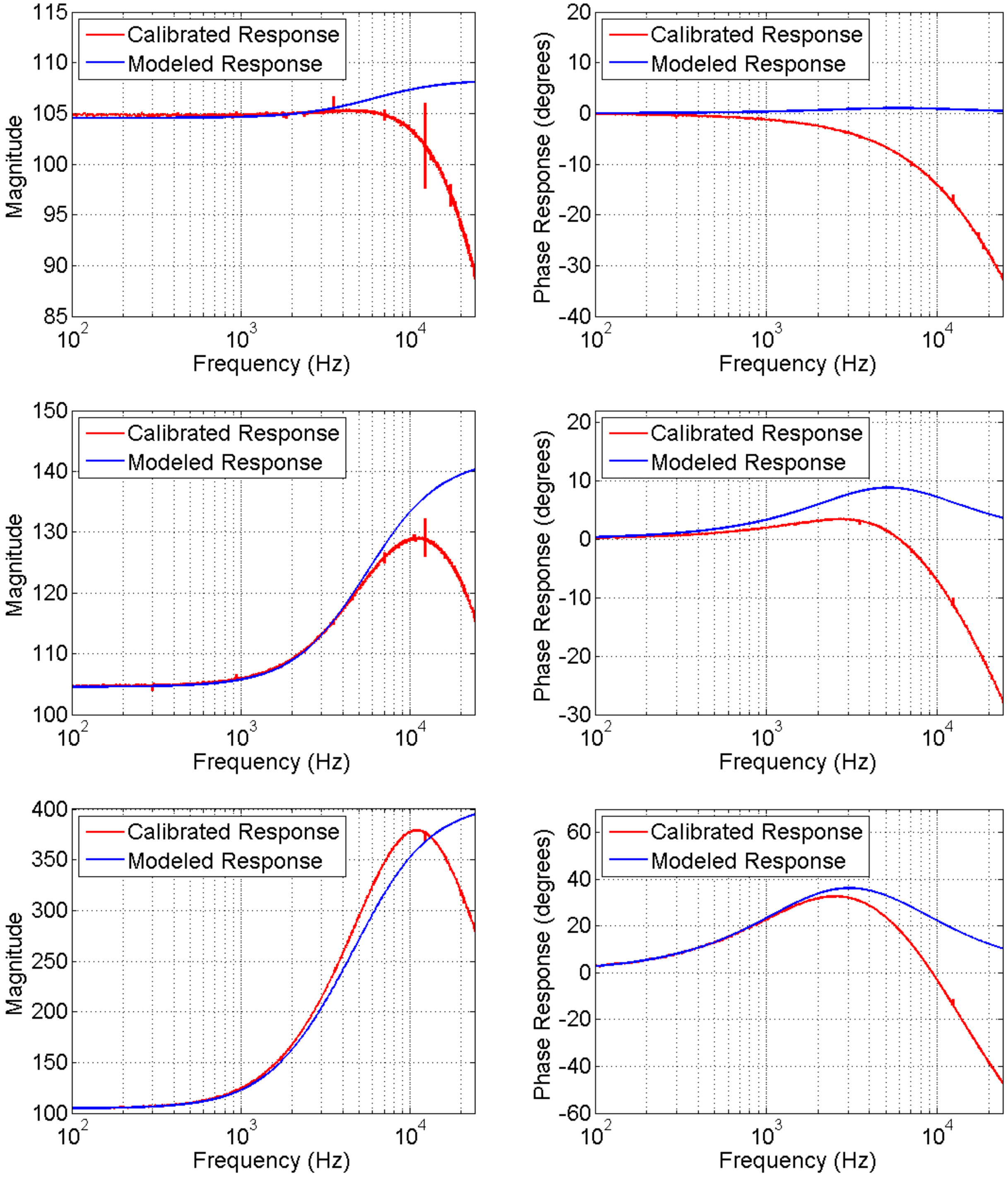

Figure 2.8: Controller calibration for high proportional gain $K_p = 105$ and $f_c = 6000$; $K_d = 0.0001$ (top); $K_d = 0.001$ (center); $K_d = 0.008$ (bottom)

2.2 Experimental Procedure

Two primary experimental methods are carried out for characterization of the frequency response of the microphone capsule. The first, acoustic calibration, is the common method for determining the frequency response of a sensor. In addition, the piezoelectric property of the membrane allows it to be electrically actuated, which yields a second method of membrane characterization, electrical calibration. It is this provision that would enable the microphones to "self-calibrate" in a beam-forming array.

2.2.1 Acoustic Calibration

Acoustic calibration takes place in a plane wave tube apparatus. Sound waves propogate down the tube perpendicularly to the tube's axis. This guarantees that the reference and prototype microphones, each mounted at the same distance down the tube, will be excited with identical acoustic pressures (in both magnitude and phase). Figure 2.9 shows a schematic of the plane wave tube setup. The plane wave tube consists of a tube with a square cross section of side length 12.7mm. This corresponds to a cut-off frequency of approximately 13.7 kHz (equivalent to an acoustic wavelength of twice the side length [8]).

A Dayton RS150S-8, 40 Watt speaker, driven by a Hafler P1000 audio amplifier, is placed at the end of the tube. The B&K reference microphone and prototype capsule are mounted in the tube so their faces are flush with the tube walls. The fiber-optic lever sensor enters the tube through a small hole opposite the prototype capsule and points at the membrane's center. The sensor is mounted on a micrometer traverse table for precise adjustment.

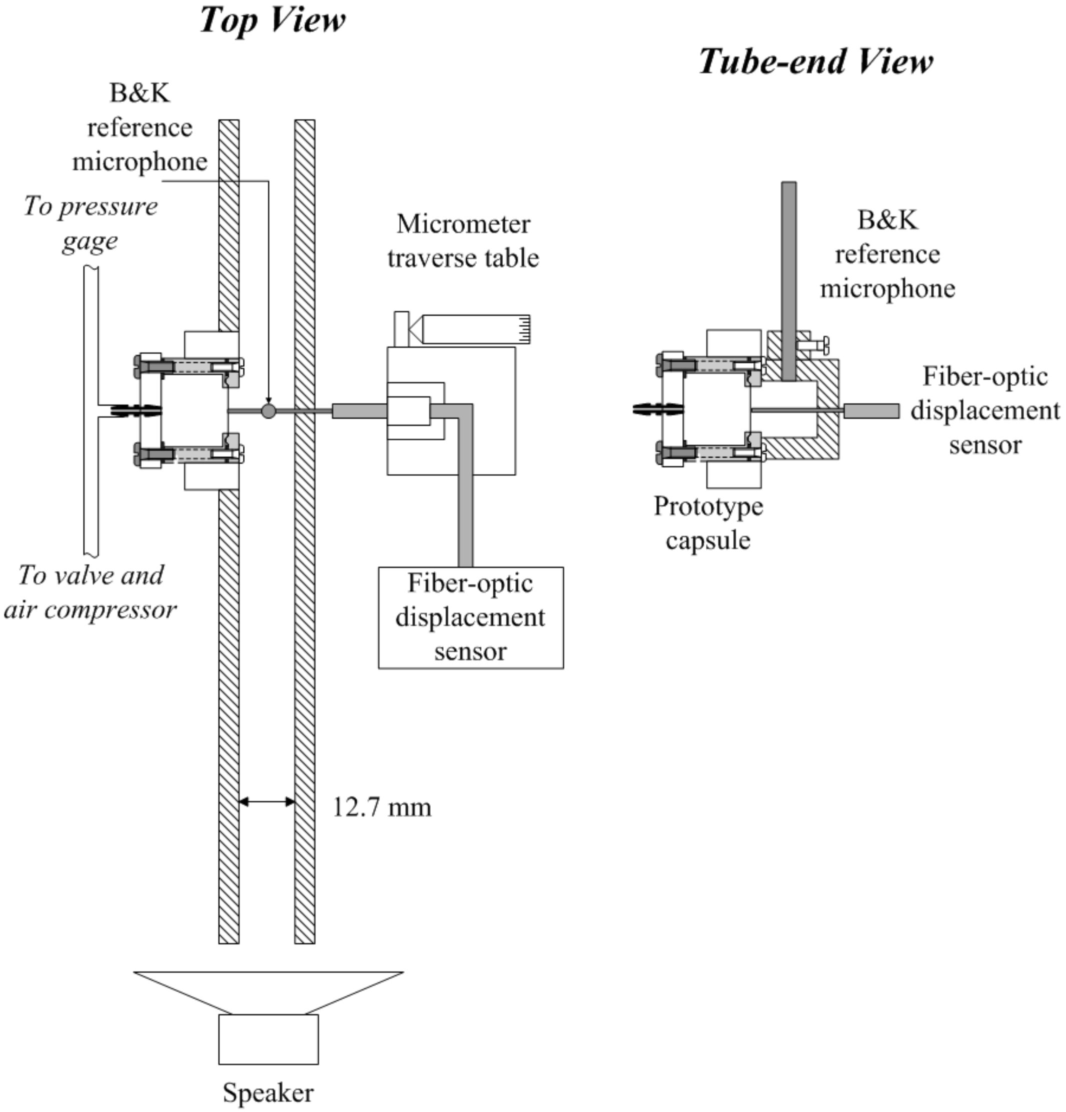

Figure 2.9: Schematic of the plane wave tube experimental setup (figure taken from [3])

For calibration of the microphone in open-loop operation, the plane wave tube is incorporated into the experimental setup shown in Figure 2.10. The optical sensor output is fed to a Larson Davis preamplifier model 2200C. The output of the amplifier is displayed on an oscilloscope, model Instek OS-653. The reference microphone used is B&K type 4938A 1/4" and is channeled through the B&K conditioning amplifier. The reference microphone signal is also viewed on the oscilloscope; and the reference microphone and feedback microphone voltages are recorded by a data acquisition board, PC-based National Instruments PCI-6024E 12-bit analog-to-digital converter (ADC), in analog input channels ai0 and ai1, respectively. The ADC is capable of acquiring up to 8 multiplexed channels in differential mode at a maximum sampling frequency of 200,000Hz. The speaker used to inject sound into the plane wave tube is driven by a Hafler amplifer, model P1000, coupled with a Hewlett-Packard function generator, model 33120A, which outputs white noise with 15MHz bandwidth.

A typical characterization experiment is initiated by turning on the function generator and amplifier and increasing the volume level to a reasonably loud setting without any clipping of the amplified signal (detected when an LED indicator light on the amplifier front panel is lit). The Philtec optical sensor is brought close to the microphone membrane in its near-field range to a value of around 2.5 volts, near the center of its linear range.

Data are then recorded using a LabVIEW program called "Mic-Plate Calibration_V3_SimpleDAQ.vi". The recorded output of the B&K and feedback microphones, which consists of 100 records of 16,384 points each, acquired at 50,000 samples per second, are analyzed as described below in section 2.3.1 to obtain the magnitude and phase response of the feedback microphone over the frequency range of interest.

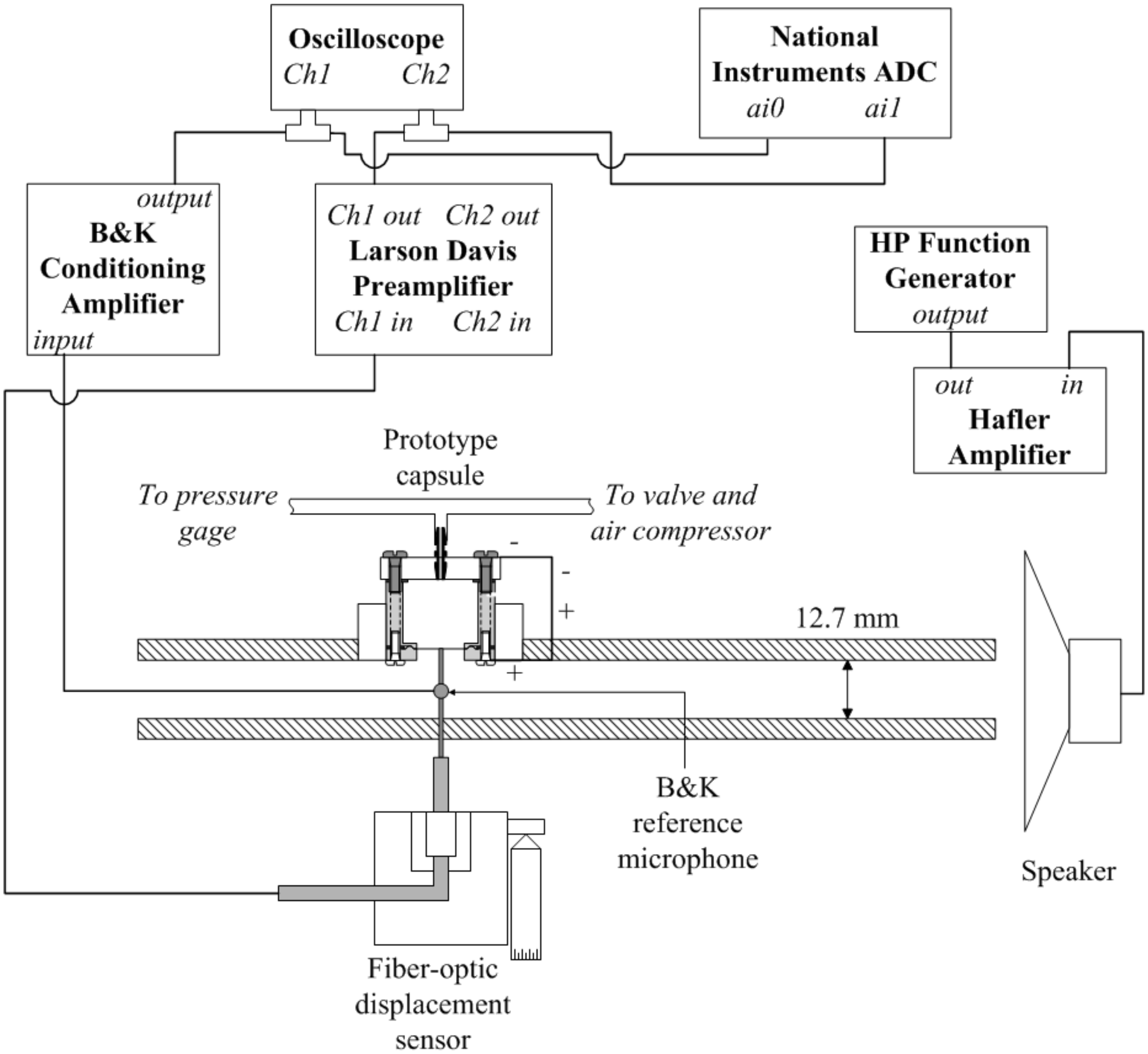

Figure 2.10: Schematic of the open-loop acoustic calibration experimental setup

The acoustic calibration setup for the microphone in closed-loop operation is similar to that of the open-loop and is shown in Figure 2.11. The main additional pieces of equipment relative to the open-loop setup are the controller and piezo driver, which are described in sections 2.1.4 and 2.1.5. During closed-loop operation, feedback gains are varied through the LabVIEW interface controlling the digital potentiometers. These gains are systematically increased until instability is reached. Three different methods of increasing gains are typically used: increasing K_d first until instability and backing off a bit followed by increasing K_p to just before instability, increasing K_p first until instability and backing off a bit followed by increasing K_d to just before instability, and increasing K_p and K_d simultaneously until just before instability. Throughout all testing, f_c is kept at a predetermined fixed value.

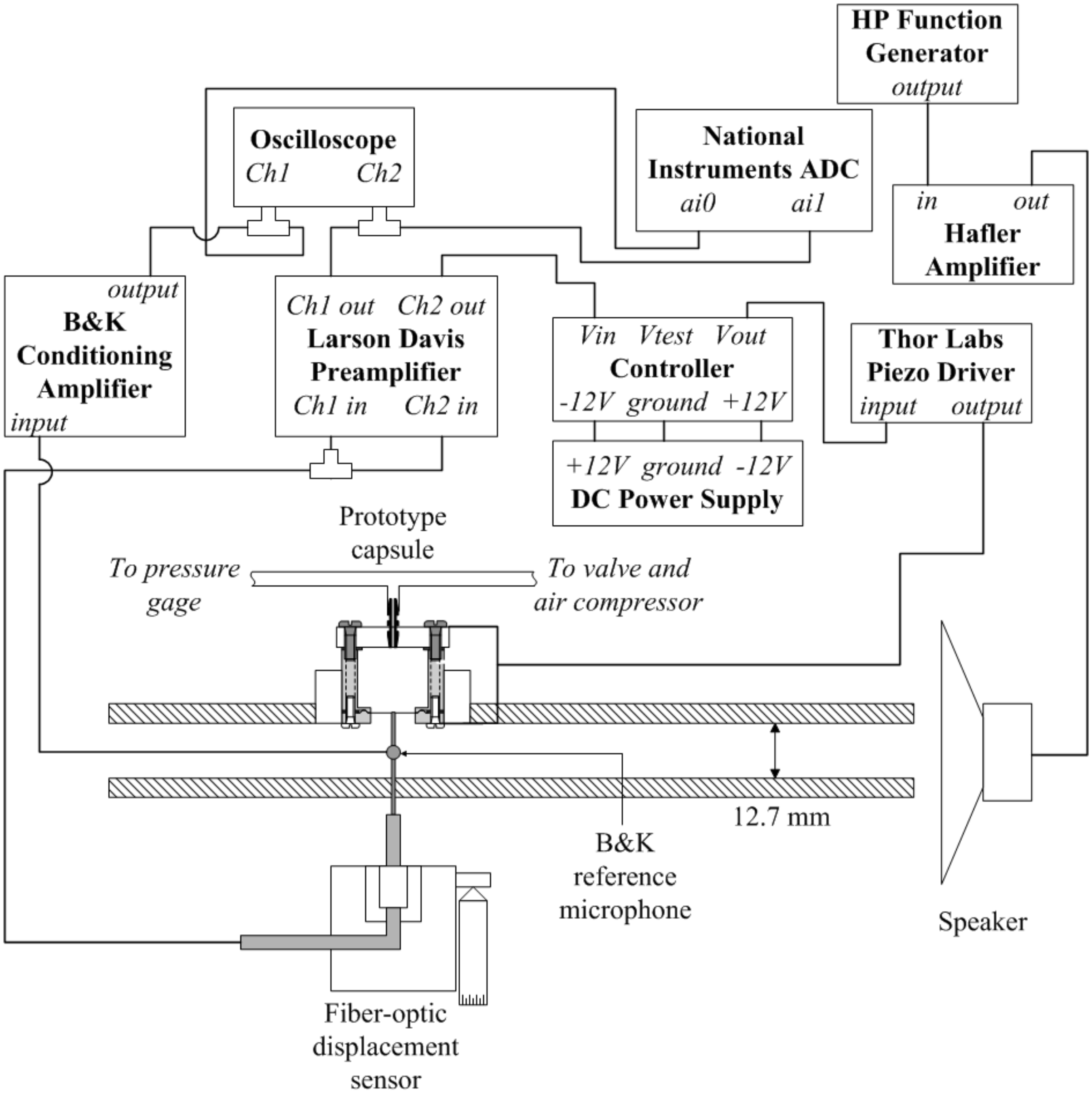

Figure 2.11: Schematic of the closed-loop acoustic calibration experimental setup

2.2.2 Electrical Calibration

A second means for calibrating the microphone is made possible by the piezoelectric capability of PVDF. By applying a sinusoidal sweep voltage across the membrane over the desired calibration frequency range, the membrane deflection amplitude and phase can be obtained at different frequencies yielding the open-loop characterization. The sweep signal represents an "equivalent" piezoelectric pressure, and hence it replaces the B&K microphone output as the reference signal in the calibration process. The setup for this test is diagrammed in Figure 2.12. For this test, the microphone is mounted outside the plane wave tube to avoid exciting tube resonances, which could affect the membrane deflection and hence the calibration, by the sound generated from membrane movement.

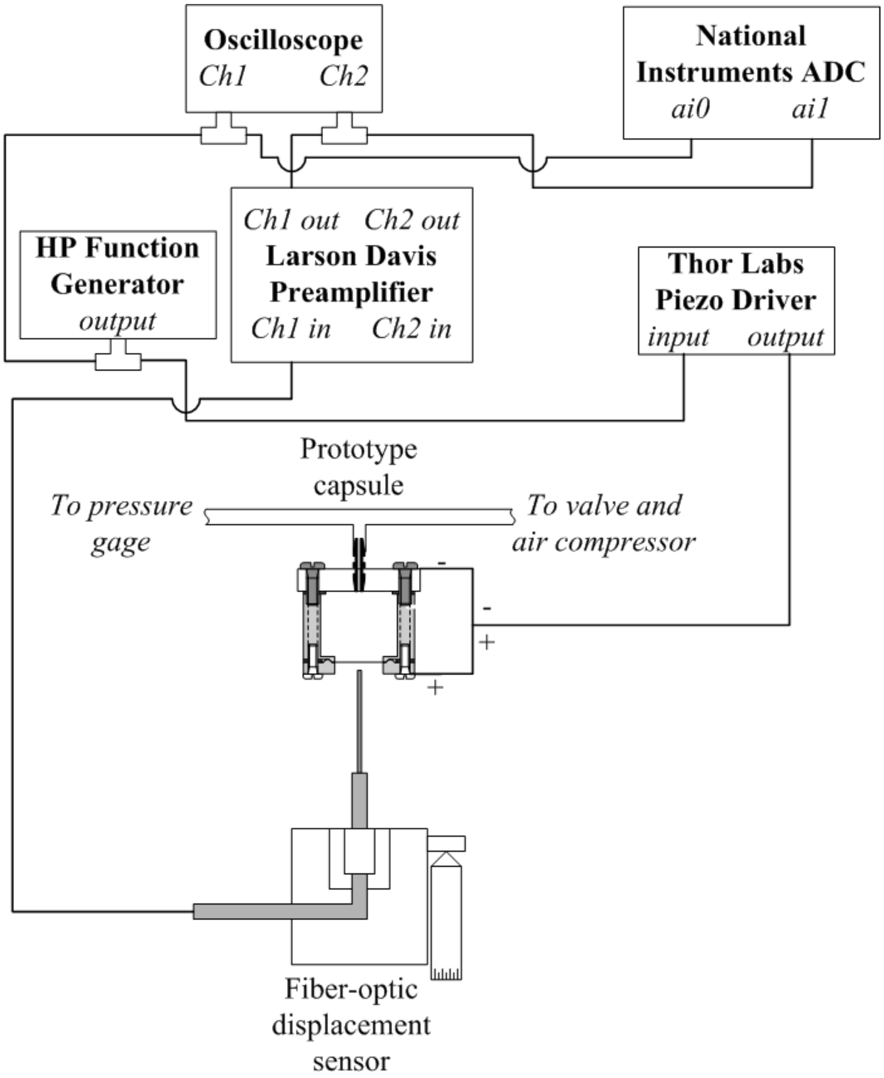

Figure 2.12: Diagram of the open-loop electrical calibration experimental setup

For closed-loop electrical calibration, the setup in Figure 2.13 is used. Here, a sinusoidal sweep voltage from the function generator is input as a test voltage to the controller (input v_{test} in Figure 2.6) and is recorded in addition to the input from the optical sensor fed through the Larson-Davis preamplifier using the ADC.

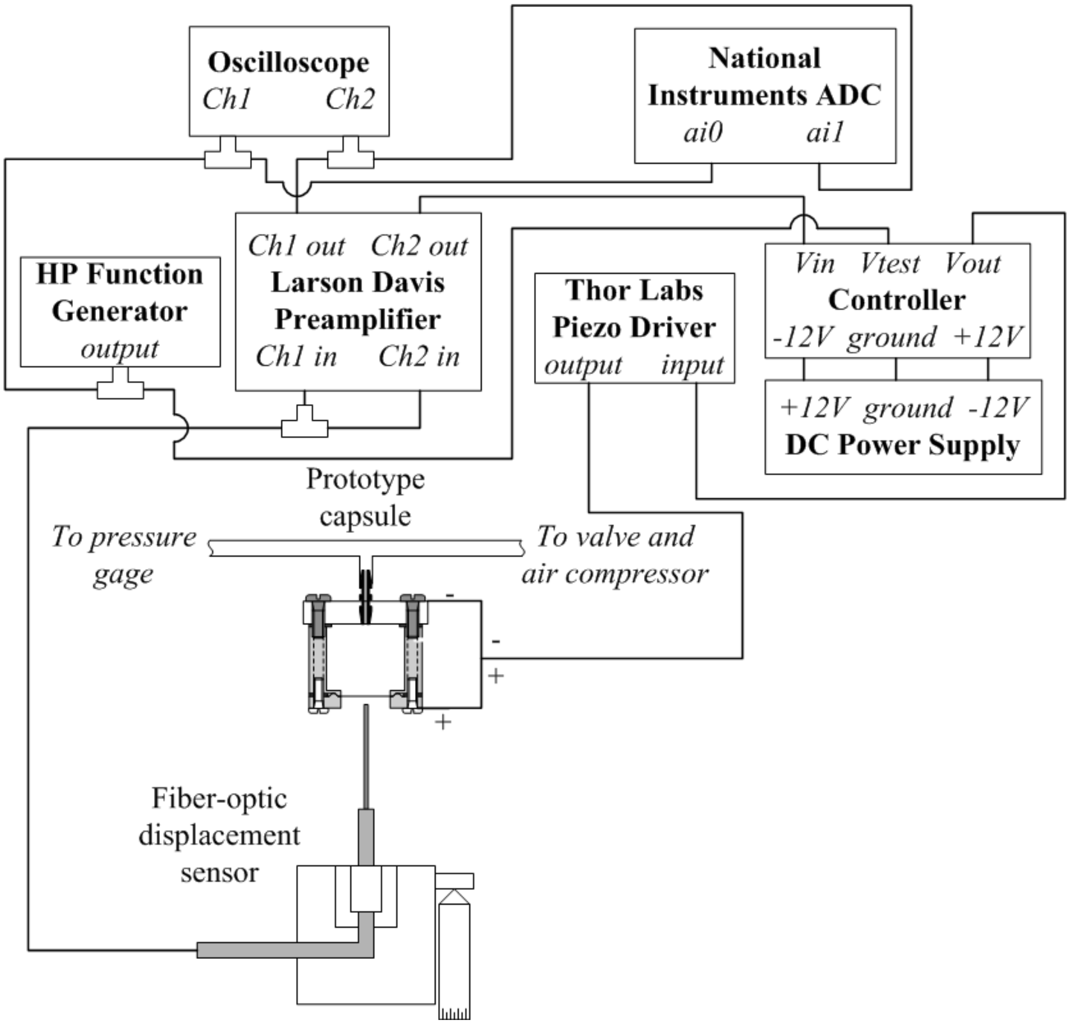

Figure 2.13: Diagram of the closed-loop electrical calibration experimental setup

2.3 Analytical Methods

2.3.1 Digital Signal Processing

In all of the calibration experiments, two signals are sampled—that of the reference signal (either the reference microphone's output voltage for the acoustic tests or the function generator's output for the electrical tests), and the voltage from the fiber-optic lever displacement sensor measuring the prototype microphone membrane's deflection. These signals are digitized using an analog-to-digital converter (ADC).

Through analysis in the frequency domain, the cross power spectrum for the two signals as well as the auto power spectrum are each computed. If $X = |X|e^{j\phi x}$ $(j = \sqrt{-1})$ is the Fourier transform of the reference signal x and $Y = |Y|e^{j\phi y}$ is the Fourier transform of the microphone signal y, the transfer function of the prototype sensor is given by the division of the cross spectrum and auto spectrum, demonstrated in equation (2.3).

$$H = \frac{XY*}{XX*} = \frac{|Y|}{|X|}e^{j(\phi x - \phi y)} \tag{2.3}$$

When the complex result of equation (2.3) is broken into polar components, the magnitude and phase of the prototype sensor are obtained and can be plotted for a range of frequencies. Note that in practice, the cross and auto spectrum are obtained from averaging those obtained from 100 records with each record containing 16,384 points sampled at 50,000Hz. This yields a frequency resolution of 3.05Hz, Nyquist frequency of 25,000Hz, and random uncertainty of 10%.

2.3.2 Membrane Model

The PVDF membrane can be modeled with the linear wave equation for a stretched membrane, given in equation (2.4).

$$T\nabla^2 z + p = \rho_S \frac{\partial^2 z}{\partial t^2} \tag{2.4}$$

where T, z, p, and ρ_S represent membrane tension, displacement, acoustic pressure, and surface density. After an assumption that the membrane undergoes axi-symmetric parabolic deflection (up to the fundamental resonance frequency) and knowing that displacement is measured at the center, z_C, equation (2.5) can be used to describe the motion, where a is the membrane radius.

$$\rho_S \ddot{z}_C + \frac{4T}{a^2} z_C = p \tag{2.5}$$

In the Laplace domain, taking center displacement as output and acoustic pressure as input, the transfer function H is given in equation (2.6), where $M = \rho_S$, $K_0 = \frac{4T}{a^2}$, and a generalized damping term C_0 is added.

$$H(s) = \frac{Z_C(s)}{P(s)} = \frac{1}{Ms^2 + C_0 s + K_0} \tag{2.6}$$

The surface density M is taken as a known constant, taken from the properties of the PVDF material. Stiffness, K_0, is related to the tension T, though T is difficult to estimate. So K_0 is calculated from the natural frequency ω_n $(2\pi f_n)$ using equation (2.7).

$$K_0 = \omega_n^2 M \tag{2.7}$$

Determination of the natural frequency is accomplished by observing the fundamental resonant frequency f_r and half-power frequencies on either side of the resonant frequency, f_1 and f_2, from the plot of the experimentally acquired frequency response. Equation (2.8) shows how the damping ratio ζ can be determined from these values.

$$2\zeta = \frac{f_2 - f_1}{f_r} \tag{2.8}$$

Knowing ζ, the natural frequency ω_n can be calculated using equation (2.9)

$$\omega_r = \omega_n \sqrt{1 - 2\zeta^2} \tag{2.9}$$

and C_0 can be determined:

$$C_0 = 2\zeta_0 \sqrt{MK_0} \tag{2.10}$$

During experimentation, multiple resonant peaks are observed, occurring at frequencies predicted for the axi-symmetric modes of a circular membrane. The model includes these modes since they are a cause of instability in the feedback system. A modified membrane transfer function is given in equation (2.11) with $C_m = (\omega_m/\omega_0)^2 C_0$, $K_m = (\omega_m/\omega_0)^2 K_0$, and ω_m/ω_0 representing the resonant frequency ratios for the higher order axi-symmetric modes calculated from vibration theory and listed, for example, in [8].

$$H(s) = \frac{Z_c(s)}{P(s)} = \sum_{m=0}^{N-1} (-1)^m \frac{1}{Ms^2 + C_m s + K_m} \tag{2.11}$$

2.3.3 Closed-Loop Modeling

One advantage of the feedback-controlled microphone is the ability to tune the microphone's response. Given that one use of the microphones is in array applications where response matching is crucial, being able to predict the closed-loop response from given open-loop parameters and controller gain settings is important.

The closed-loop transfer function, based on the block diagram depticted in Figure 2.5, is given is follows:

$$W_{cl}(s) = \frac{V(s)}{P(s)} = \frac{H(s)G_O(s)}{1 + H(s)G_O(s)G_C(s)G_{PZ}(s)} \tag{2.12}$$

Employing the denominator of equation (2.12) as the characteristic equation, a pole placement method was used in [3] to design the controller to achieve a certain desired fundamental resonant frequency and damping for the closed-loop response. A similar method was not utilized here because the main interest was in determining the limits of instability of the sensor rather than arriving at a desired response.

The following results show how the original microphone design performs. Chapters 3 and 4 on the added provisions of damping and area-averaged sensing respectively will demonstrate the improvement in the operational range of the microphone that each of these methods offers.

2.4 Baseline Results

2.4.1 Internal Static Pressurization

An induced curvature in the membrane is known to improve the piezoelectric response of the membrane (i.e. deflection per unit applied voltage) [4], [5], [6]. In the present work, this is achieved by pressurizing the back chamber of the microphone as described in section 2.1.2. To select a value for the chamber pressure, internal static pressurization tests were performed. The changes in actuation sensitivity (S_e) and resonant frequency (f_n) of the PVDF membrane were determined for several internal pressurizations using electrical calibration and the results are plotted in Figure 2.14.

Based on the responses shown in Figure 2.14, an internal static pressurization of 2kPa is chosen for all characterization tests of the microphone. This pressurization yields a significant increase in the actuation sensitivity with no substantial increase in resonant frequency.

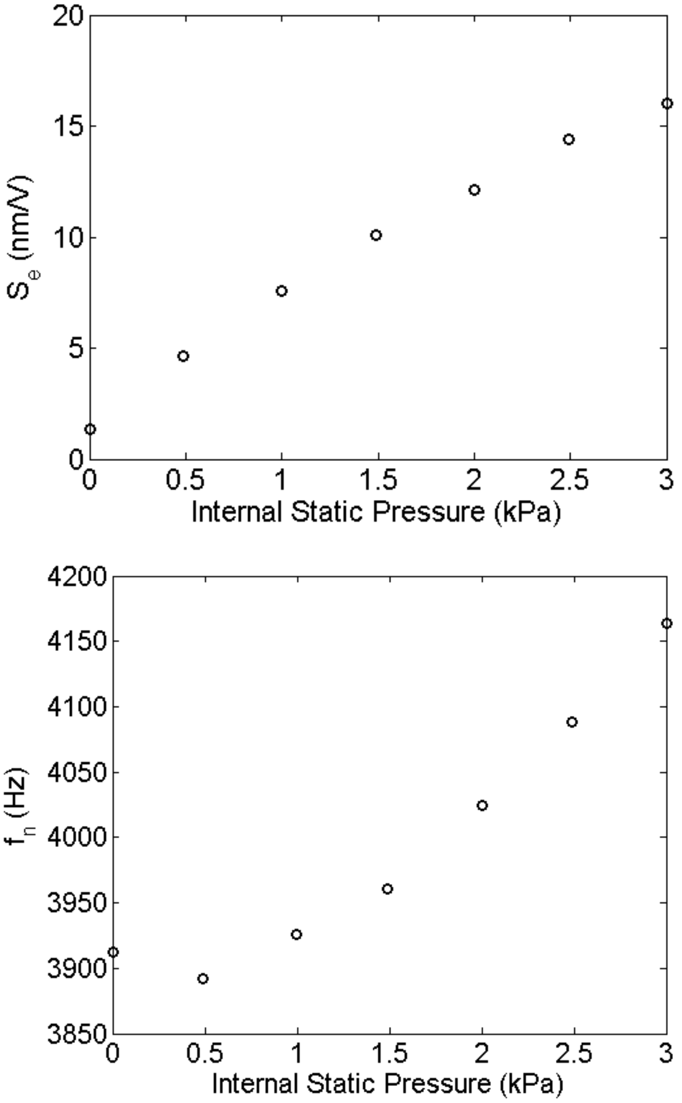

Figure 2.14: Electrical response of PVDF membrane for various internal static pressurizations; actuation sensitivity of PVDF membrane (top); fundamental resonant frequency (bottom)

2.4.2 Open-Loop Characterization

Figure 2.15 shows the open-loop characterization for the undamped microphone, both acoustic and electrical calibration. The two methods of characterization yield similar responses, as expected. Therefore the electrical open-loop calibration is used from this point forward. It gives a smoother response, eliminating the small steps seen in the acoustic response, believed to be due to acoustic reflections in the plane wave tube.

Figure 2.16 shows the electrical characterization alone with the open-loop model determined using the method in section 2.3.2.

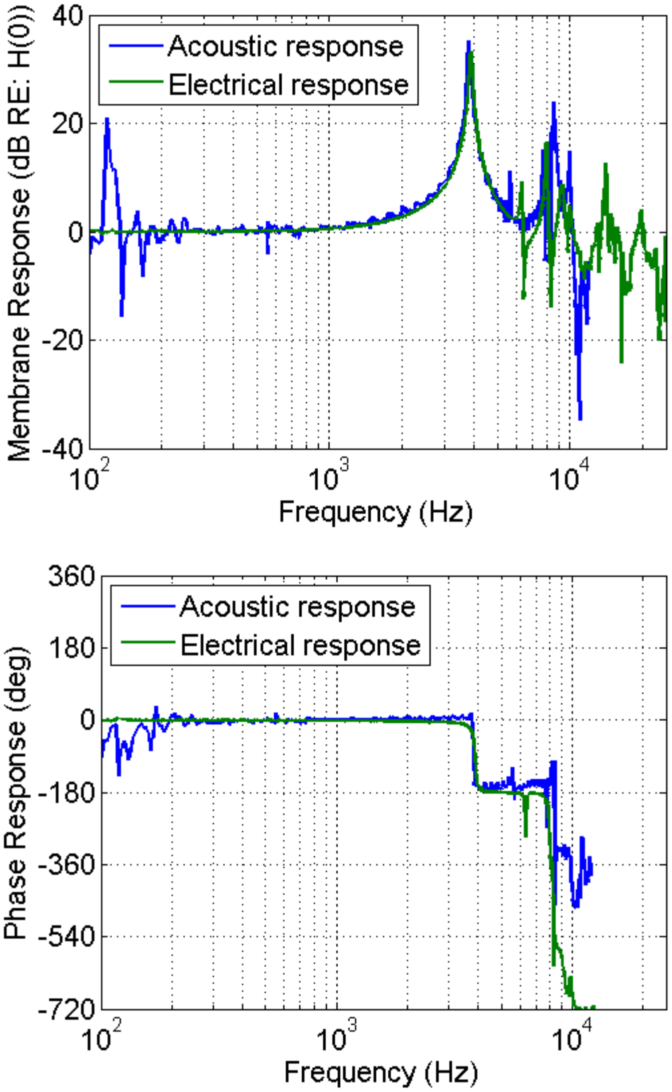

Figure 2.15: Open-loop characterization for the undamped microphone; magnitude (top); phase (bottom)

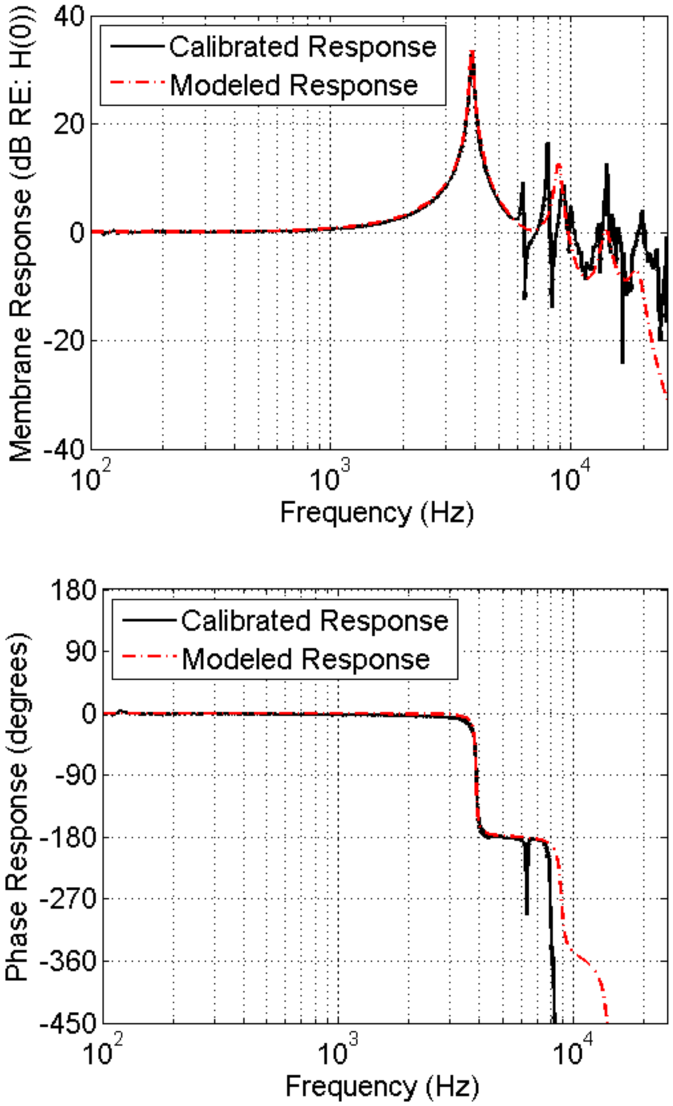

Figure 2.16: Open-loop electrical characterization for the undamped microphone with model; magnitude (top); phase (bottom)

2.4.3 Closed-Loop Characterization

As with the open-loop characterization, calibrations were performed acoustically and electrically for the closed-loop case. As described in section 2.2, the gains were systematically increased in three different patterns. Figure 2.17 compares the acoustic and electrical responses. In this case, the electrical and acoustic calibrations were both performed with the microphone mounted in the plane wave tube. It can be seen from Figure 2.17 that the two methods of characterization yield similar results, just as with the open-loop. Therefore, focus will be on using the electrical calibration method because it is simpler and can be used over a wider bandwidth than the plane wave tube.

Figures 2.18–2.20 show the electrical response plotted with the model curve predicted using equation 2.12 coupled with the knowledge of the open-loop parameters, feedback gains, and transfer function of the lever sensor. The figures correspond to the three methods of increasing the gains, described in the closed-loop calibration procedure of section 2.2, while setting f_C to a fixed 6000 Hz. This value for f_C is somewhat arbitrary; it was chosen to be slightly higher than the open-loop microphone's natural frequency so the influence of K_d would be limited to the frequency range up to f_C. Overall, the results in Figures 2.18–2.20 show an alteration in the microphone's response, as demonstrated, for example in the increase in the natural frequency of the closed-loop microphone. The specific values of the natural frequencies can be found in Table 2.3. For reference, the natural frequency of the open-loop microphone is 3980 Hz. It should be noted that the results in Figures 2.18–2.20 represent the baseline closed-loop microphone response against which the response of the microphone with added damping provision and with an area-averaging sensor will be compared in Chapters 3 and 4, respectively.

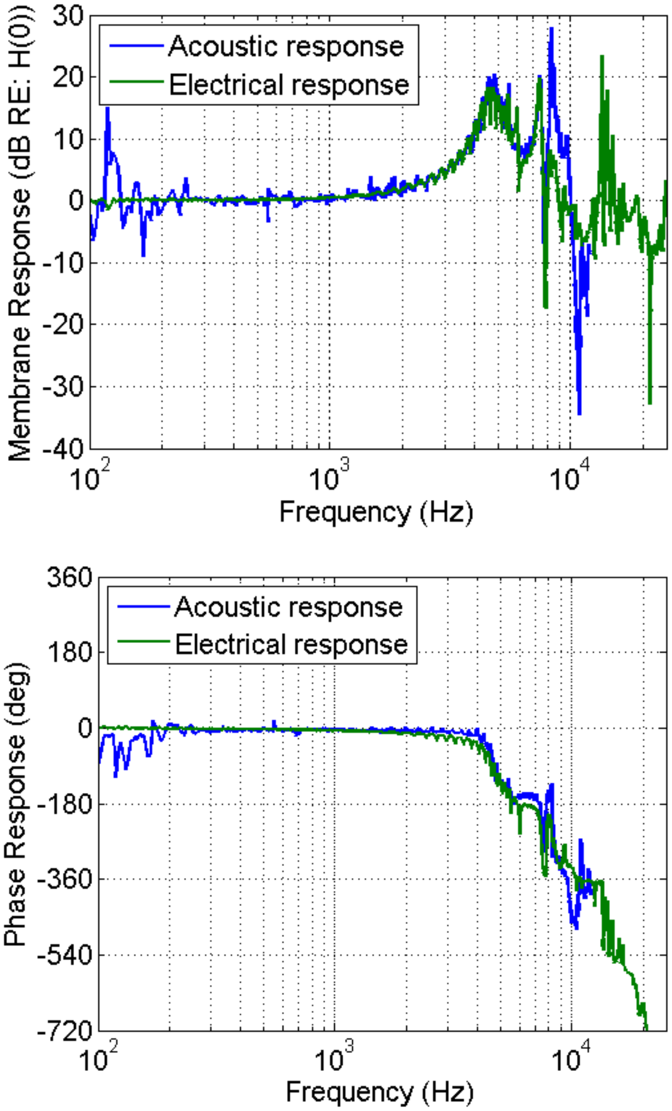

Figure 2.17: Closed-loop characterization for the undamped microphone increasing K_P first ($f_C = 6000$ Hz); magnitude (top); phase (bottom)

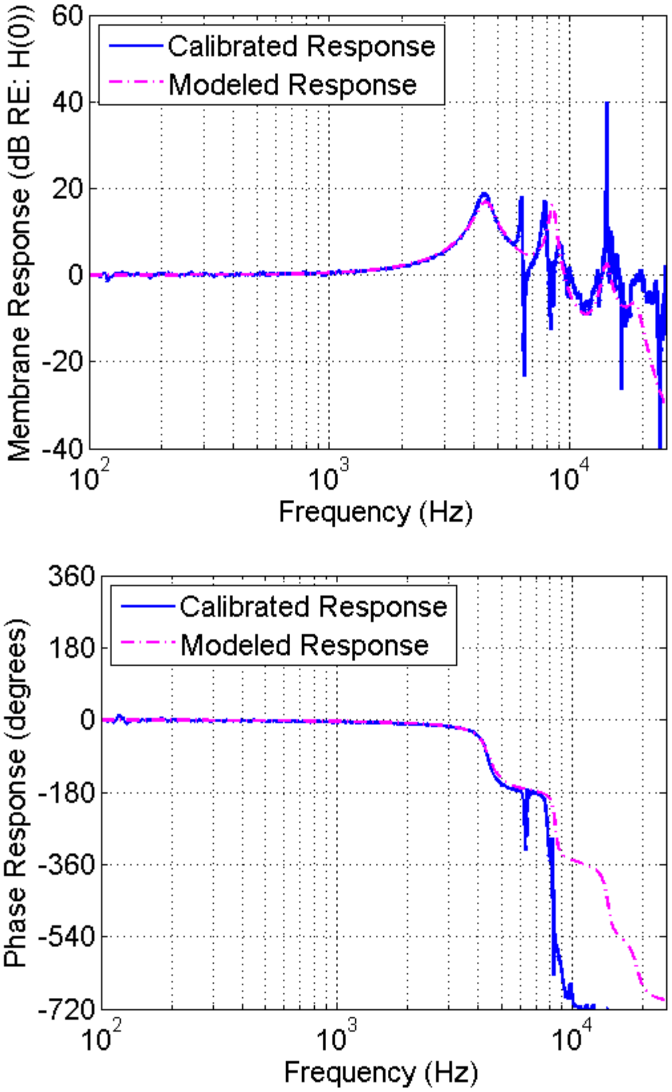

Figure 2.18: Closed-loop characterization for the undamped microphone increasing K_p first ($f_C = 6000$ Hz); magnitude (top); phase (bottom)

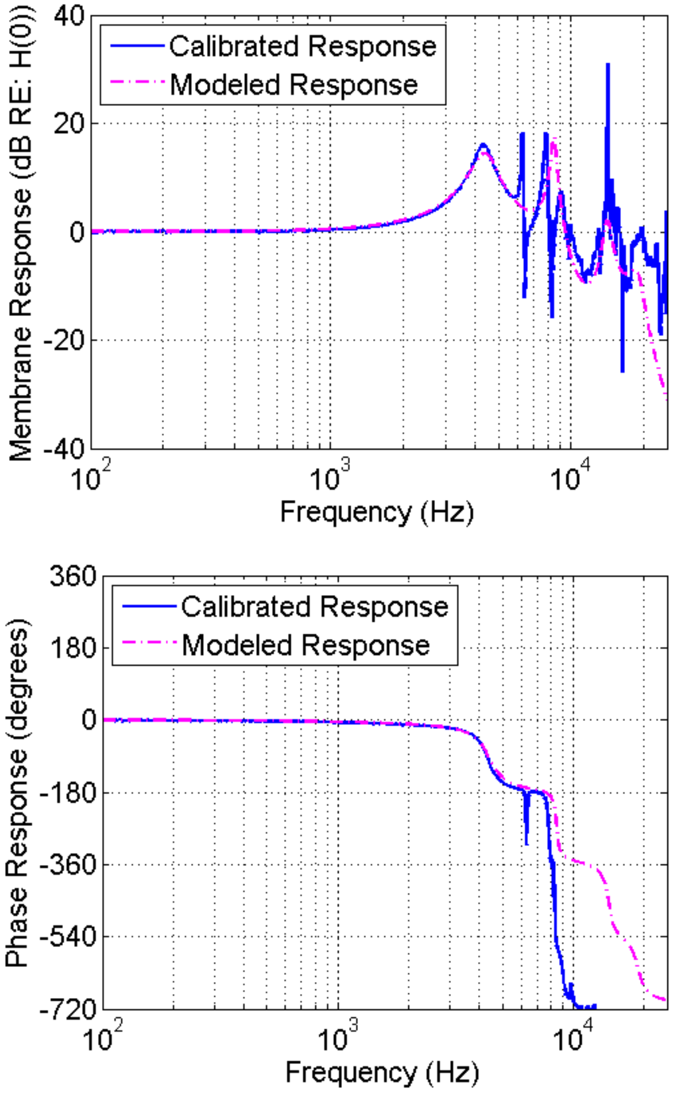

Figure 2.19: Closed-loop characterization for the undamped microphone increasing K_d first ($f_c = 6000$ Hz); magnitude (top); phase (bottom)

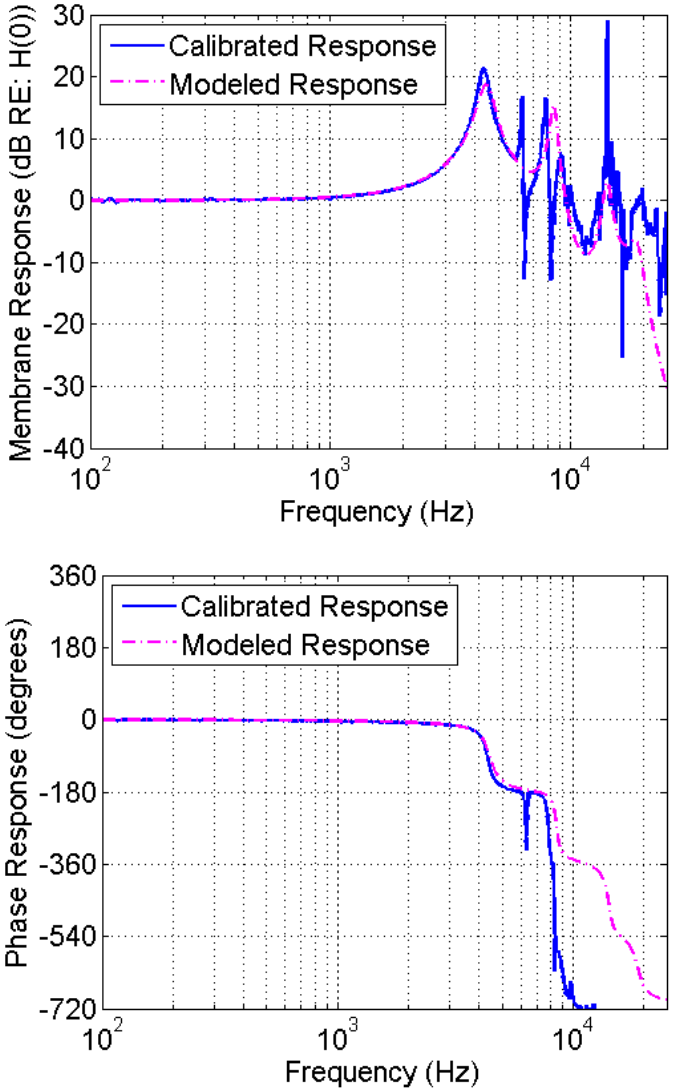

Figure 2.20: Closed-loop characterization for the undamped microphone increasing K_p and K_d simultaneously ($f_c = 6000$ Hz); magnitude (top); phase (bottom)

The closed-loop calibrations were repeated for two other values of f_C. Because the value of 6000 Hz was somewhat arbitrary, both higher and lower values (3000 and 10,000 Hz respectively) were tested. The higher value of 10,000 Hz did not produce substantial change in the microphone's response, and hence the results are not included here. On the other hand, the calibration results for $f_C = 3000$ Hz are shown in Figures 2.21–2.23 for the three methods of increasing gains. Lowering the value of f_C produced some improvement in the results, when improvement is defined as higher closed-loop natural frequencies.

Table 2.3: Natural frequencies for the undamped microphone in closed-loop operation for different values of f_C

	Increase K_P first	Increase K_d first	Increase together
Natural frequency for $f_C = 6000$ Hz	4414	4309	4336
Natural frequency for $f_C = 3000$ Hz	4490	4506	4417

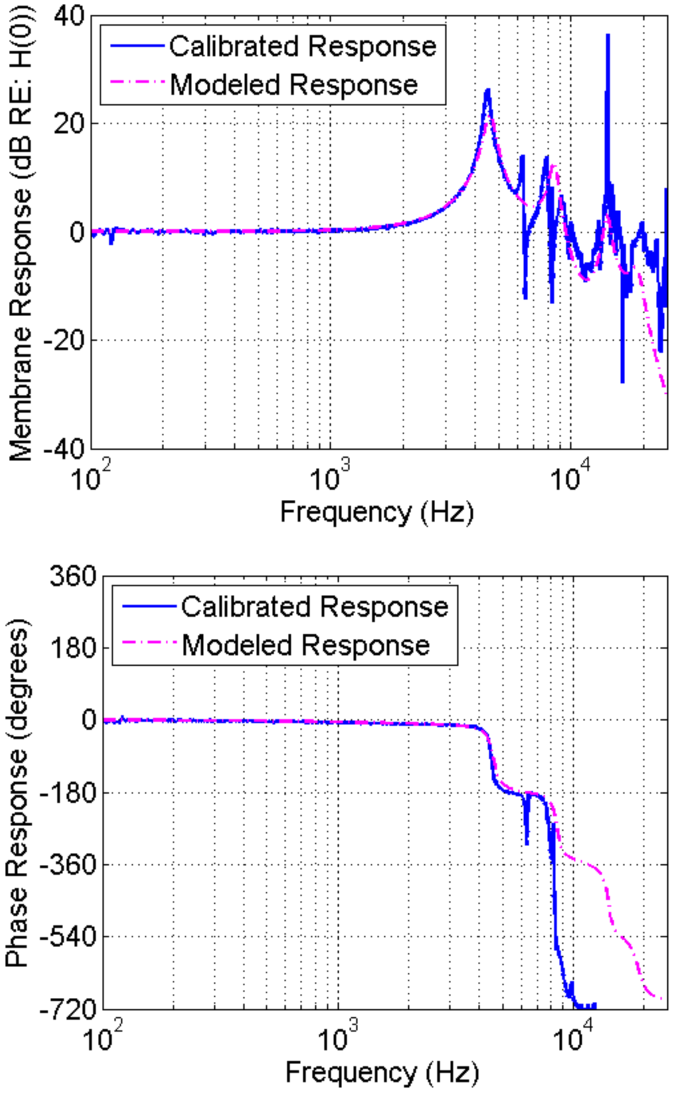

Figure 2.21: Closed-loop characterization for the undamped microphone increasing K_p first ($f_C = 3000$ Hz); magnitude (top); phase (bottom)

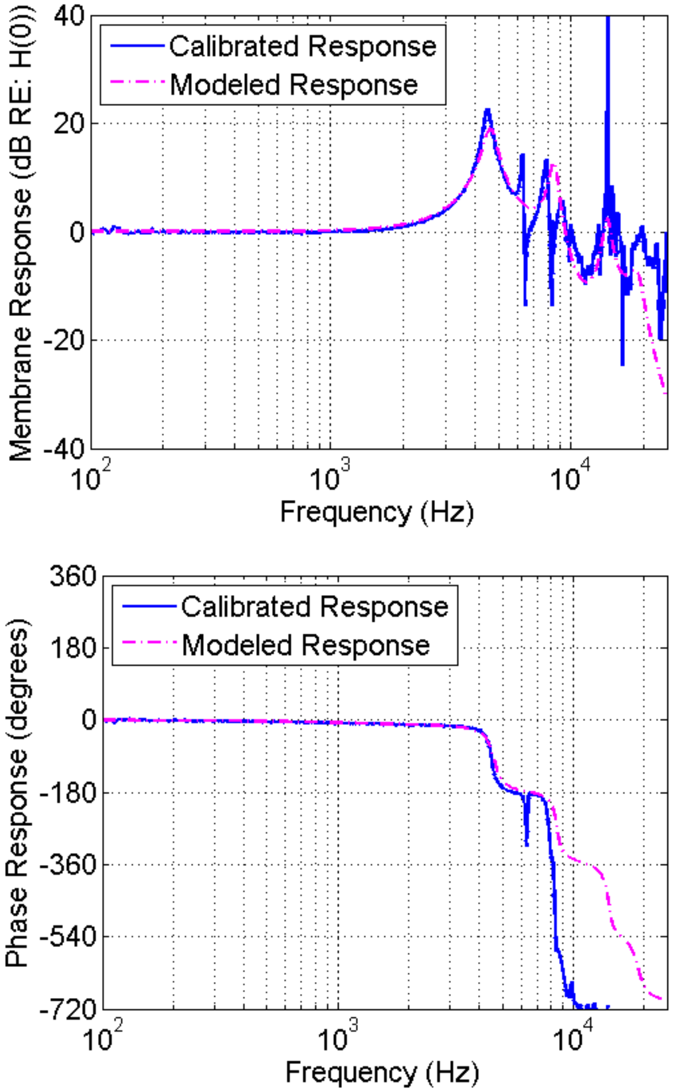

Figure 2.22: Closed-loop characterization for the undamped microphone increasing K_d first ($f_C = 3000$Hz); magnitude (top); phase (bottom)

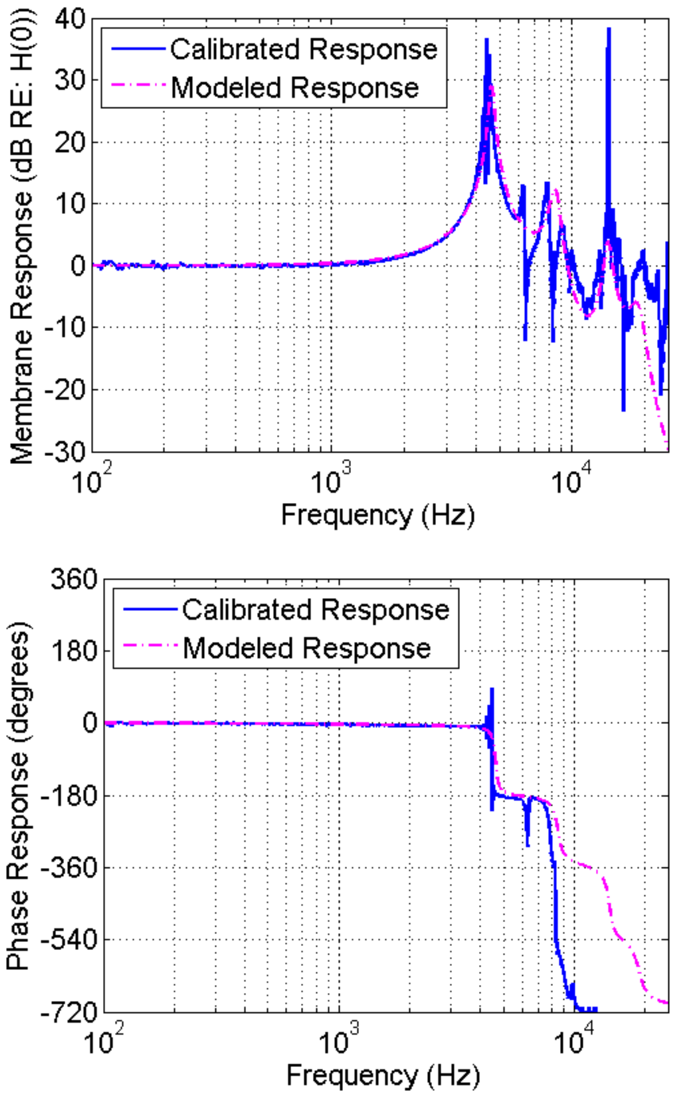

Figure 2.23: Closed-loop characterization for the undamped microphone increasing K_p and K_d simultaneously (f_c = 3000Hz); magnitude (top); phase (bottom)

Chapter 3

Damping Provisions in the Microphone Back-Plate to Extend Operational Range

In Chapter 2, a feedback-controlled microphone was discussed. Though the microphone has the unique advantages of 'self-calibration' and response matching to other similar types of microphones, controller instability caused by high-order resonance peaks limits the ability to increase the fundamental resonance frequency through feedback. To address this, a microphone with mechanical damping provisions was constructed and tested for increase in stability and operational range of the microphone.

3.1 Analytical Modeling of a Perforated Back-Plate

A method for decreasing the strength of the membrane resonances is the addition of perforated back-plates. These are similar to the concept of back-plates found in commercial condenser microphones. A rigid back-plate with small diameter holes has been incorporated into the microphone design. This back-plate sits a distance of 1mm behind the membrane, as seen in Figure 3.1. As acoustic pressure from an incoming sound causes the membrane to oscillate, air is forced through the holes and the associated viscous friction causes losses which in turn results in damped membrane motion.

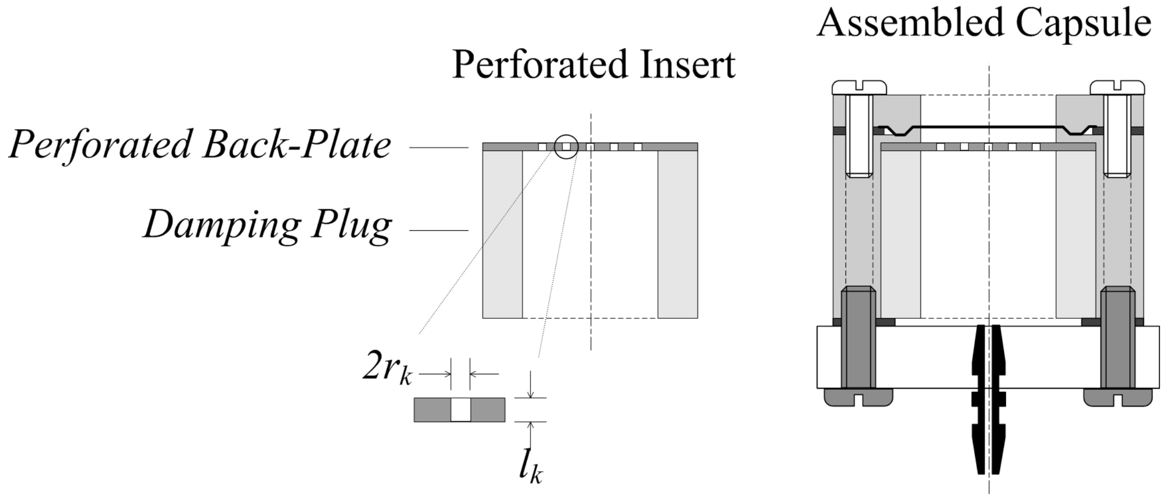

Figure 3.1: Perforated-insert-plug design (left) and microphone capsule with plug inserted (right)

Holes with known diameter and depth are used because a model is available to give the predicted damped response for the membrane. This model is based on work done by Zuckerwar [7] with additional assumptions and simplifications used by Radcliffe [3]. Details of the model can be found in these references; however, essential traits are summarized here for completeness. The model is based on electrical-circuit analogy, in which each hole is modeled as a resistance and an inductance in series. The parallel network of such elements is then connected in series with a capacitor representing the air chamber behind the perforated plate. The simplifying assumptions introduced in [3] include assuming that the membrane has piston-like motion and that air movement through all holes is identical. Through the analysis outlined in [3], it is shown that the resisting pressure due to the influence of the back-plate can be modeled as an added effective inertial mass, M_{0b}, damping, C_{0b}, and stiffness, K_{0b}. For a hole length of l_k and a hole radius of r_k (see Figure 3.1), these expressions are given in equations (3.1), (3.2), and (3.3):

$$M_{0b} = 0.4314 \cdot A \frac{\rho_0 (l_k + 1.7 r_k)}{q \pi r_k^2} \tag{3.1}$$

$$C_{0b} = 0.4314 \cdot A \frac{(8 \omega_0 \rho_0 \mu)^{1/2}}{q \pi r_k^2} \left(1 + \frac{l_k}{2 r_k} \right) \tag{3.2}$$

$$K_{0b} = 0.4314 \cdot A \frac{\gamma \rho_0 c_T^2}{V_b} \tag{3.3}$$

where A is the membrane surface area, ρ_0 is air density, q is the number of holes, ω_0 is the membrane natural frequency, μ is the air viscosity, γ is the specific heat ratio, c_T the isothermal speed of sound through air, and V_b is the capsule back chamber volume. When these terms are added to the membrane transfer function, they modify it as follows:

$$H(s) = \frac{1}{(M + M_{0b}) s^2 + (C_0 + C_{0b}) s + K_0 + K_{0b}} \tag{3.4}$$

3.2 Damping Back-Plate Fabrication

The damping back-plates are thin, disc-like components that are mounted in the capsule so that they sit approximately 1mm back from the membrane. The current design involves a cylindrical plug on which the damping back-plate disc is mounted using superglue and the resulting assembly is inserted into the microphone capsule design depicted in Figure 3.1. A mechanical stop for the top of the plug is used to position the damping back-plate at the correct distance from the membrane. The plug is easily removed from the capsule, giving the ability to switch between back-plates with different hole layout patterns efficiently.

3.2.1 Design of Hole Layouts

Using the model described in section 3.1, some designs for the damping back-plate's layout were created. Based on analysis in [3], in order to effectively design a perforated back-plate with minimal effective mass, a very small hole radius, r_k, is ideal. In this way, one can increase the damping while minimizing the reduction of the resonance frequency. Accordingly, different ways of making very small holes (smaller than 0.25mm diamter, the limit with conventional drilling techniques) were investigated. Limitations based on manufacturability forced the hole depth-to-diameter ratio ($l_k/2r_k$) to a maximum of 1. This limitation is for a laser ablation technique, determined as the most cost-effective available method for fabricating damping back-plates and described in 3.2.2. Other methods considered included microfabrication, but available facilities were tooled for thin-film microfabrication, not for bulk micromachining applications as necessary for the back-plate fabrication. Also, using a porous material instead of creating holes in a solid material was considered, but this method would not allow the model described in section 3.1 to be utilized and a systematic design approach would not have been possible.

A MATLAB program with GUI interface created by Radcliffe [3] was utilized in determining the size and number of holes for the back-plate designs. Back-plates were designed for half-inch, three-eighths-inch, and quarter-inch microphone membrane sizes. However, in the present study, only half-inch sensors are characterized. Figure 3.2 shows a screenshot of the GUI, with the design for the half-inch diameter membrane. The membrane parameters on the lefthand side of the GUI—Diameter, Surface Density, Damping Ratio, and Edge Tension—as well as the back-plate parameters—Hole Diameter, Hole Length, # of Holes, and Back. Volume—are all input parameters. The membrane parameters M, C, and K as well as the air layer parameters are all GUI output values. The input membrane parameters are found from electrical calibration of the open-loop response as described in Chapter 2. The plot shown at the bottom of the GUI is the magnitude frequency response plot. The black line is the calibration of the membrane without damping, used to obtain the membrane input parameters to the model, and the red line is the prediction of the model with the added damping.

The hole dimensions were chosen as 0.1mm diameter and 0.1mm hole depth, based on the laser ablation process. To yield visibly damped resonance peaks while keeping the natural frequency near the open-loop for the undamped microphone, the targeted damping ratio was 0.1. The holes were laid out in two different configurations: concentric circles and a hexagonal layout. Letting the geometry govern the design, back-plates with 91 and 121 holes were created. Table 3.1 summarizes the back-plate designs for the half-inch microphone sensor size, including the resulting damping ratio based on the predictions of the MATLAB code. The coordinates of the hole centers for the three back-plate layouts are included in Appendix A for reference. Figure 3.3 shows a sketch of back-plates with circular and hexagonal hole layout geometry.

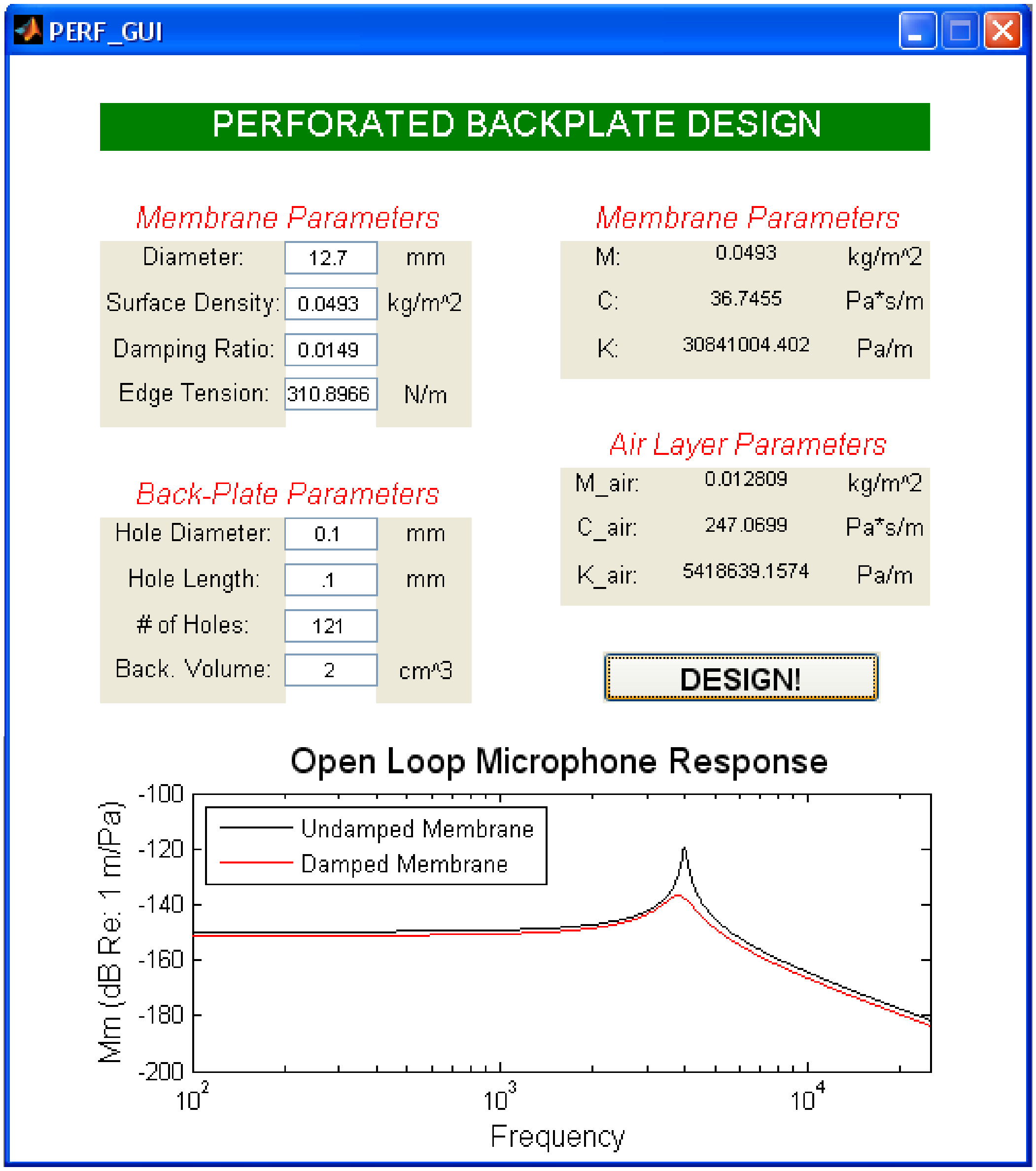

PERFORATED BACKPLATE DESIGN

Membrane Parameters
Diameter: 12.7 mm
Surface Density: 0.0493 kg/m^2
Damping Ratio: 0.0149
Edge Tension: 310.8966 N/m

Back-Plate Parameters
Hole Diameter: 0.1 mm
Hole Length: .1 mm
# of Holes: 121
Back. Volume: 2 cm^3

Membrane Parameters
M: 0.0493 kg/m^2
C: 36.7455 Pa*s/m
K: 30841004.402 Pa/m

Air Layer Parameters
M_air: 0.012809 kg/m^2
C_air: 247.0699 Pa*s/m
K_air: 5418639.1574 Pa/m

Figure 3.2: "Perforated back-plate design" MATLAB GUI for designing hole layouts

Table 3.1: Damping back-plate designs for the half-inch microphone capsule

	Half-Inch Diameter Capsule		
Number of holes (q)	91	91	121
Hole layout geometry	hexagonal	circular	circular
Predicted damping ratio ζ	0.1161	0.1161	0.0946

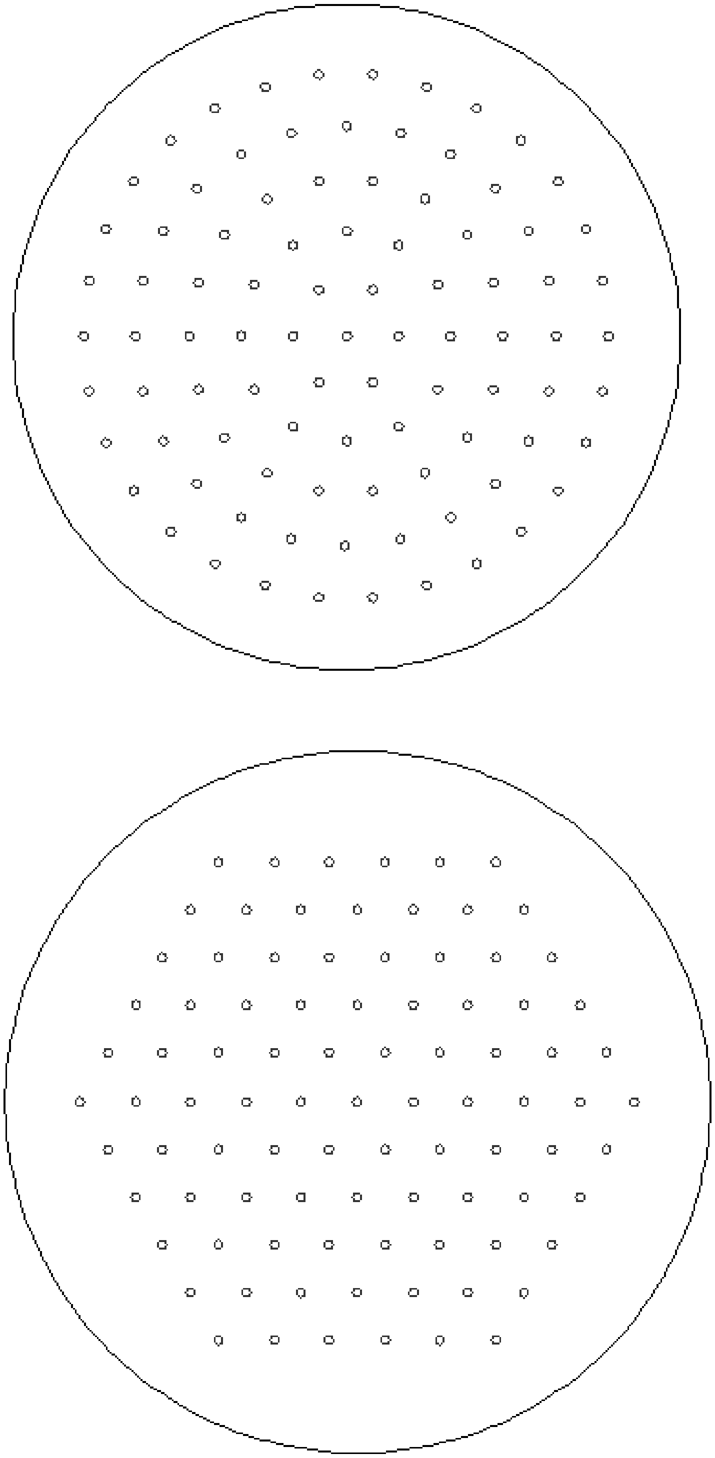

Figure 3.3: Sketches of damping back-plates with a circular and a hexagonal hole layout pattern

3.2.2 Laser Ablation Method

Laser ablation is a method by which solid material is removed by a laser. This was done at NASA Langley Research Center (LaRC) in the Fabrication Technology Development Branch. The material, aluminum in the case of the back-plates, absorbs the energy and sublimates. For the damping back-plates, the hole outlines were traced by the laser, and afterward, a circular outline was drawn around the outside to cut out a disc-shaped back-plate from the aluminum sheet. The pattern was read from an AutoCAD .dwg file. The laser ablator follows the lines in the order they are drawn, so care must be taken to create the holes in the AutoCAD drawing in the correct sequence. Also, the beamwidth of the laser must be taken into account; for a beamwidth of 0.025mm and desired hole diameter of 0.1mm, holes should be specified to 0.075mm diameter in the .dwg file.

3.3 Damped Membrane Calibration Results

3.3.1 Open-Loop Characterization

The open-loop parameters for the membrane are determined by the method described in section 2.3.2 using the baseline calibration shown in Figure 2.16. These parameters are summarized in Table 3.2 and are then used in the model from section 3.1 to determine the predicted frequency response for the half-inch microphone with the three damping inserts.

Figures 3.4–3.6 show the open-loop characterizations for the microphone with each of the three damping inserts described in Table 3.1. Plotted also are the predicted responses. These figures show that the constructed back-plates work well in damping the resonance peak substantially. It is clear that there is a deviation from the model and that the actual

Table 3.2: Membrane parameters estimated from open-loop calibration

Parameter	**Symbol**	**Value**	**Unit**
Mass	M	0.0493	kg/m^2
Damping	C_0	36.7960	$Pa \cdot s/m$
Stiffness	K_0	$30.841 \cdot 10^6$	Pa/m
Damping Ratio	ζ_0	0.0149	
Natural Frequency	f_0	3.98	kHz

damping is stronger than predicted. The model, however, gave good predictions in [3]. Some sources of lack of agreement in the current work may include that the very small hole sizes require some modification to the model. Also, perhaps the model needs to be modified to account for the small air gap between the back-plate and the membrane.

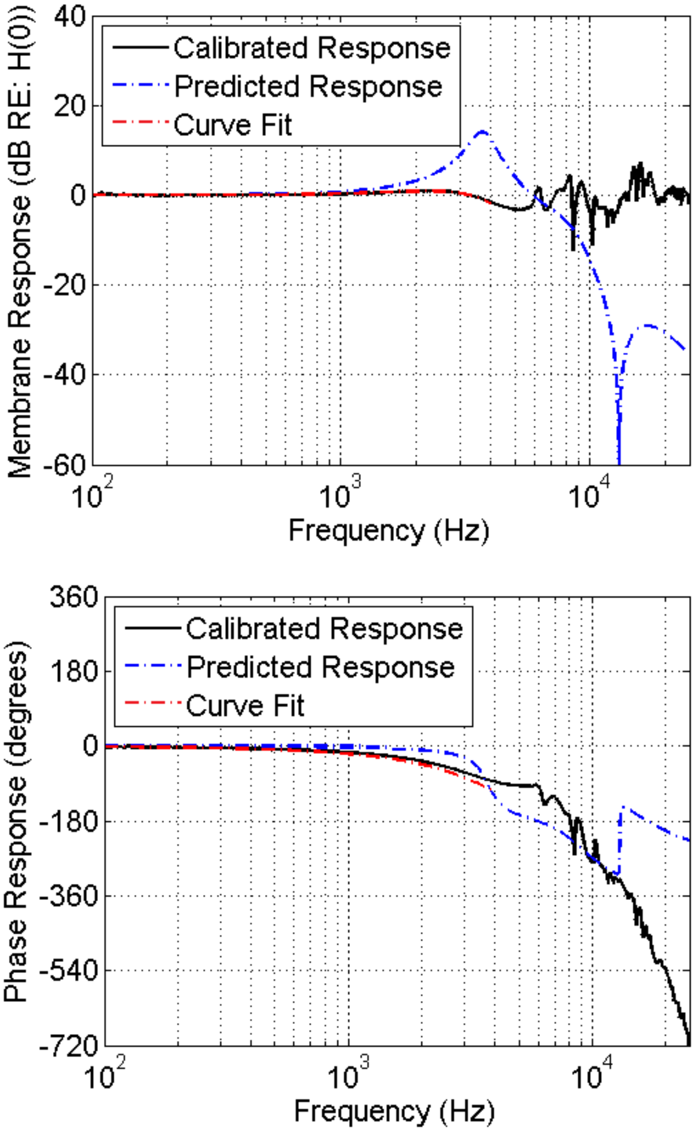

Figure 3.4: Calibrated and predicted frequency response of the microphone with 91 holes, hexagonal-arrangement damping back-plate: magnitude (top) and phase (bottom) plot

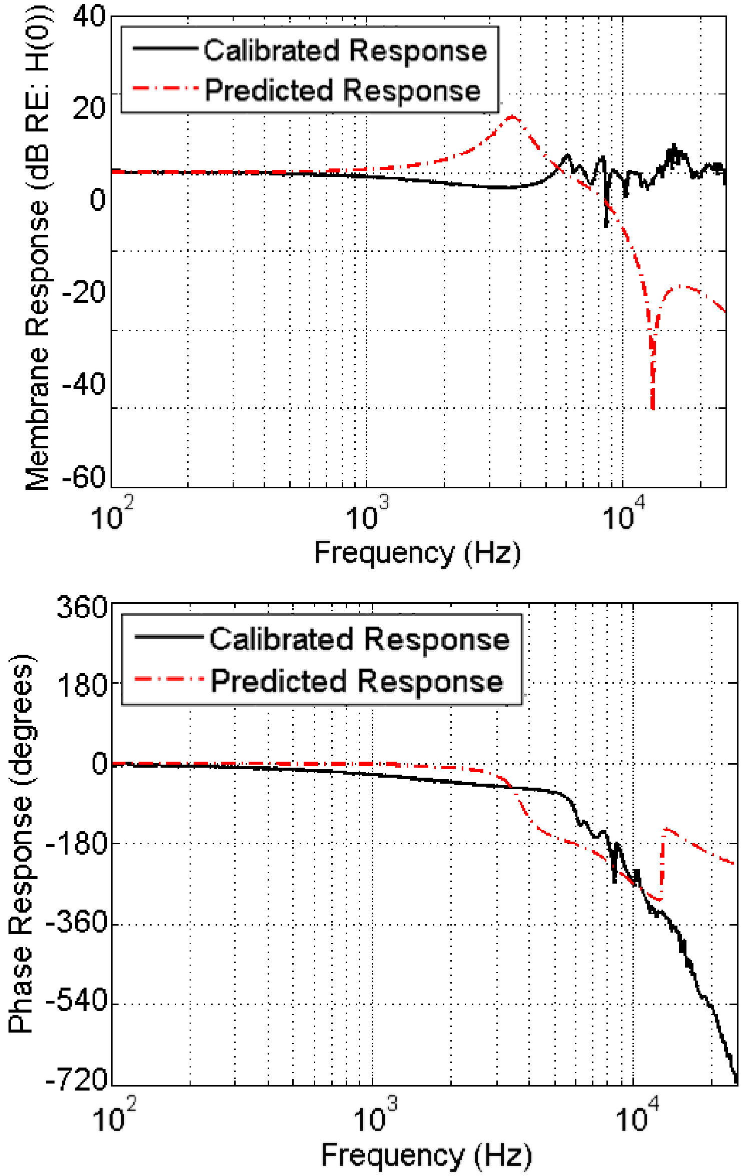

Figure 3.5: Calibrated and predicted frequency response of the microphone with 91 holes, circular-arrangement damping back-plate: magnitude (top) and phase (bottom) plot

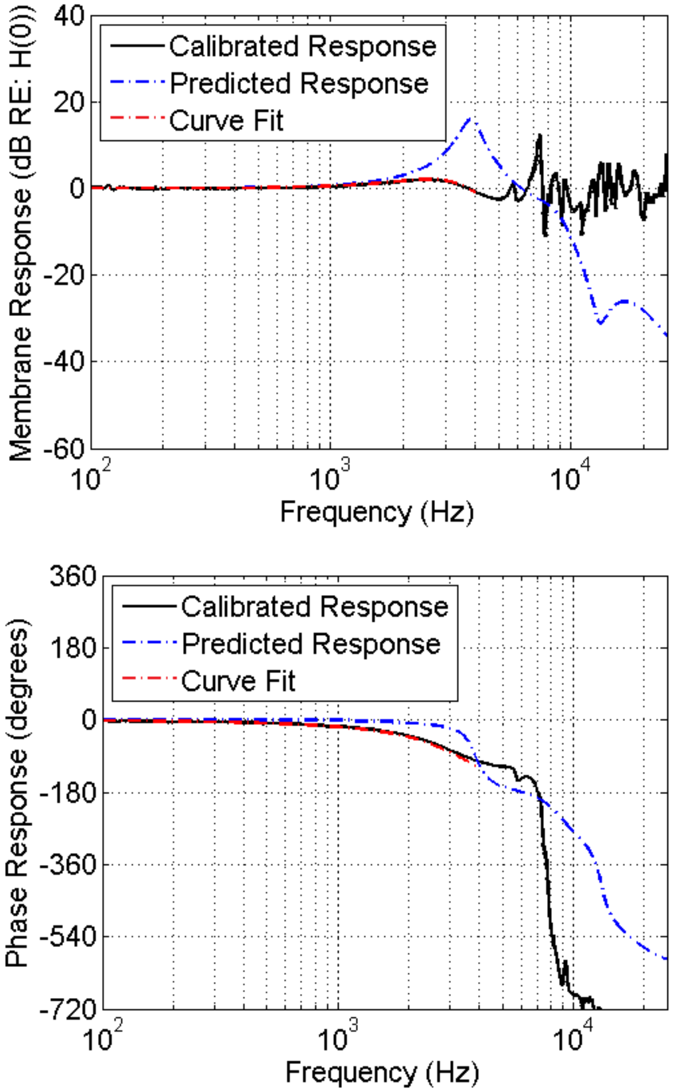

Figure 3.6: Calibrated and predicted frequency response of the microphone with 121 holes, circular-arrangement damping back-plate: magnitude (top) and phase (bottom) plot

As indicated in section 2.3.2, a lumped-parameter, second-order model represents the response of the microphone through the first resonance frequency very well and can be used to determine the stiffness, damping ratio, and resonance frequency of the membrane. To this end, such a model was fit to the responses shown in Figures 3.4–3.6. Because the resonance frequency is highly damped, the natural frequency and damping ratio estimation methods of section 2.3.2 are invalid. Instead, the second-order equation model is fit directly to the response data in order to determine the parameters of interest. To facilitate the fitting process, the expression for the amplitude for a second-order system is rearranged and a linear fit is performed on the data. Equation (3.5) gives the expression for the magnitude A of the frequency response normalized by the response at zero frequency.

$$A = \frac{1}{\sqrt{[1-(\frac{\omega}{\omega_n})^2]^2 + 4\zeta^2(\frac{\omega}{\omega_n})^2}} \tag{3.5}$$

Setting $x = \omega^2$, the expression may be rearranged as follows:

$$\frac{1}{x}(\frac{1}{A^2} - 1) = mx + b \tag{3.6a}$$

$$m = \frac{1}{\omega_n^4} \tag{3.6b}$$

$$b = \frac{2(2\zeta^2 - 1)}{\omega_n^4} \tag{3.6c}$$

Based on equation 3.6, a linear fit can be performed on data in Figures 3.4–3.6 after the dependent variable has been manipulated to match the expression on the left hand side of equation (3.6a) and the independent variable is set to ω^2. The membrane's natural frequency and damping ratio can then be determined from the slope and intercept of the fit using equations 3.6b and 3.6c. The curve fit is done over the frequency range up to 4000Hz to avoid the inclusion of data corresponding to high-order resonances, which are not represented by the second-order model. The resulting curve fits can be seen in Figures 3.4 and 3.6, drawn in red. Table 3.3 compares the damping ratio obtained from the fit to that predicted by the design model for the three cases investigated. The best fit model yielded complex numbers for the natural frequency and damping ratio of the microphone response with the back-plate with 91 holes in circular arrangement.

Table 3.3: Actual and predicted damping ratios and natural frequencies for back-plates with different hole arrangement

	91 holes hexagonal	91 holes circular	121 holes circular
$\zeta_{predicted}$	0.1161	0.1161	0.0946
ζ_{actual}	0.5697	?	0.4739
$f_{n,predicted}$ (Hz)	3721	3721	3846
$f_{n,actual}$ (Hz)	3541	?	3330

The values in Table 3.3 confirm the discrepency noted in the response plots earlier with the actual damping being larger than the damping ratio predicted from the model. The 121-hole circular pattern insert was used for further closed-loop testing. Of the three damping back-plates, it had the lowest value for the actual damping ratio, closest to the target damping value of around 0.1.

3.3.2 Feedback-Controlled Microphone Calibration Results

Figures 3.7–3.9 show the closed-loop responses for the damped microphone. Figure 3.7 shows the characterization with K_p increased first. Figure 3.8 shows the characterization with K_d increased first. And Figure 3.9 shows the characterization with K_p and K_d increased simultaneously in small increments. Here, all the results are done for $f_c = 3000$.

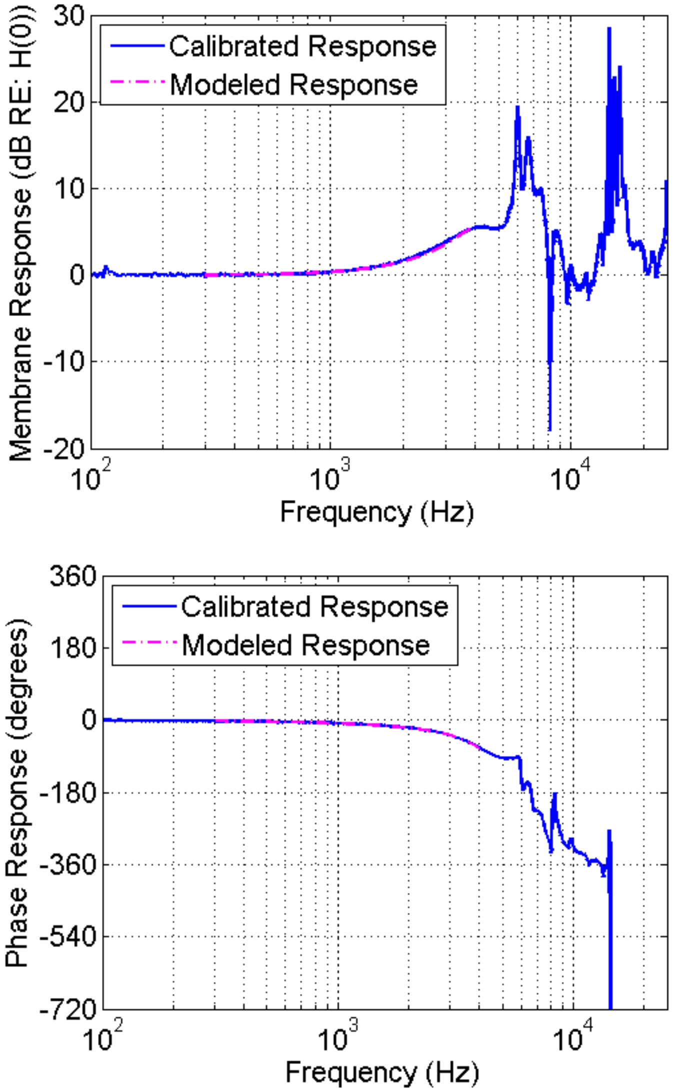

Figure 3.7: Closed-loop characterization for damped microphone increasing K_P first; magnitude (top); phase (bottom)

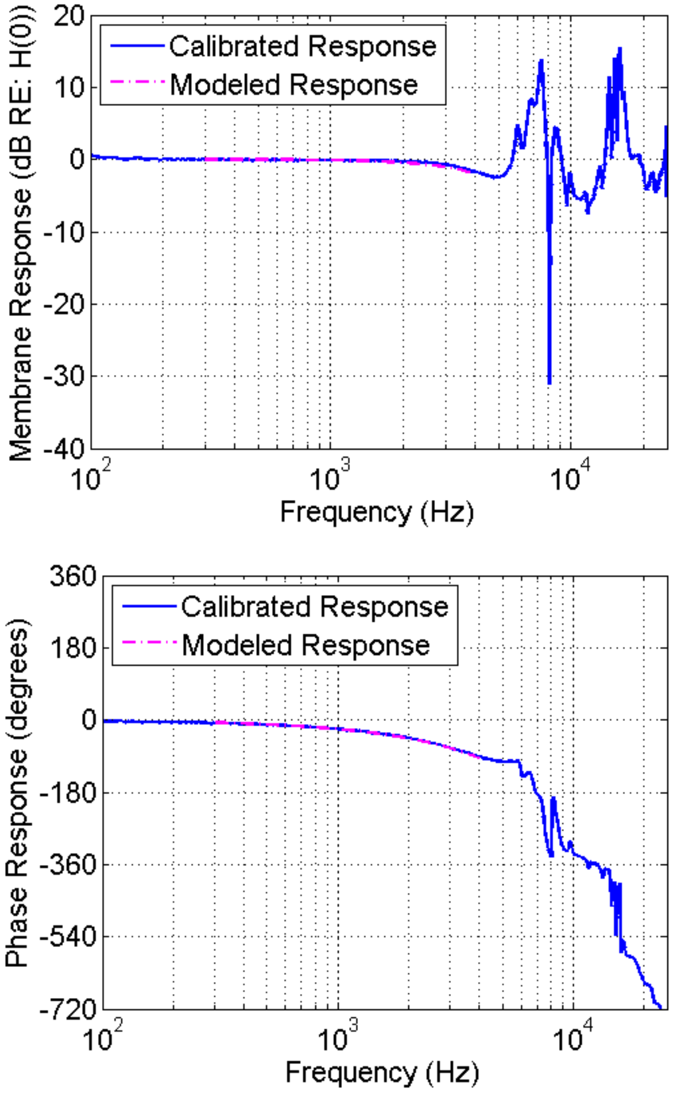

Figure 3.8: Closed-loop characterization for damped microphone increasing K_d first; magnitude (top); phase (bottom)

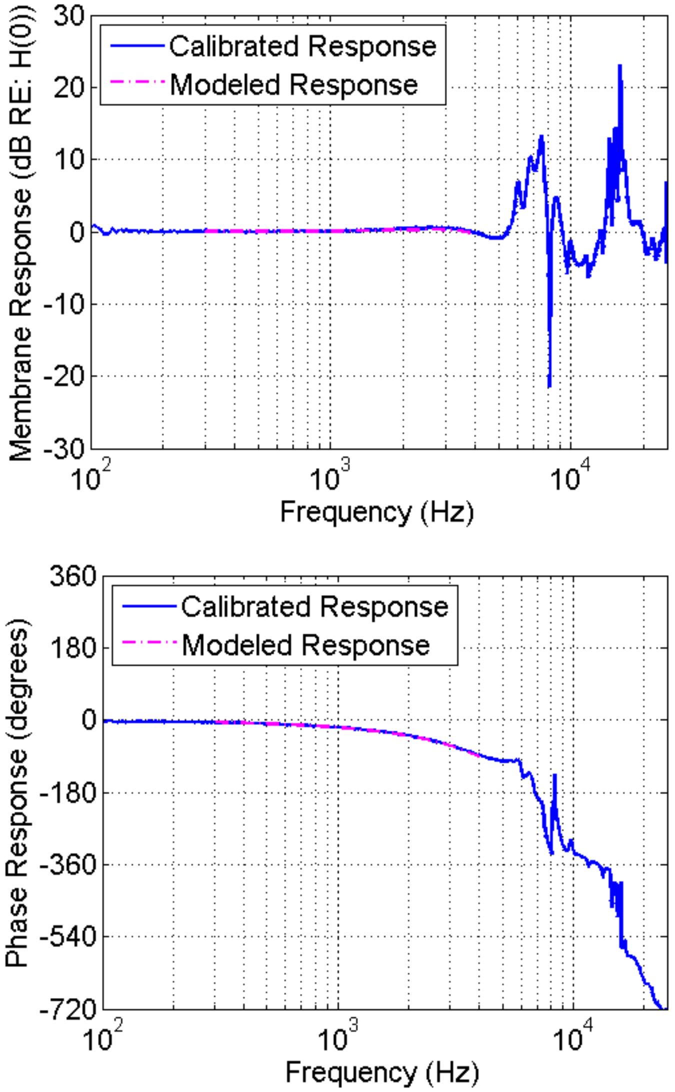

Figure 3.9: Closed-loop characterization for damped microphone increasing K_p and K_d simultaneously; magnitude (top); phase (bottom)

3.4 Evaluation of Feedback-Controlled Microphone Results and Extension of Operational Range

The increase of operational range for the closed-loop operation of the microphone is examined and compared. Specifically, the extent of change that can be exerted on some metric of the microphone's response through the feedback is assessed quantitatively. One method to compare stability range is by measuring the increase in natural frequency of the membrane. For the undamped-microphone case with a clear fundamental resonance peak, the method described in section 2.3.2 is used to extract the natural frequency and damping ratio from the data plotted in Figures 2.18–2.20, and the damping ratios and natural frequencies are summarized in Table 3.4. For the damped-microphone case, there is not a strong resonant peak and a best fit model is used, as described in section 3.3.1. The models were developed from the closed-loop, damped microphone electrical calibration results plotted in Figures 3.7–3.9. Damping ratio and natural frequency values are summarized in Table 3.5.

Table 3.4: Natural frequencies and damping ratios for the undamped microphone in open- and closed-loop operation

	Open Loop	Closed Loop		
		Increase K_p first	Increase K_d first	Increase together
Natural frequency f_n (Hz)	3862	4490	4506	4417
Damping ratio ζ	0.0149	0.0219	0.0327	0.0091

In Tables 3.4 and 3.5, it is observed that the closed-loop method of increasing K_d first has the highest natural frequency for both the undamped- and damped-microphone cases. For the undamped microphone, closed-loop operation is able to increase the natural frequency by up to 16.7%, while for the damped microphone, the natural frequency increases up to

Table 3.5: Natural frequencies and damping ratios for the damped microphone in open- and closed-loop operation

	Open Loop	Closed Loop		
		Increase K_p first	Increase K_d first	Increase together
Natural frequency f_n (Hz)	3432	4278	5181	4659
Damping ratio ζ	0.4885	0.3187	0.7911	0.6170

51.0% during closed-loop operation. This is a significant improvement in the microphone stable operational range due to the addition of the damping back-plate.

Another mode of comparison between the damped and undamped microphones is to compare the controller gains attained before the operation became unstable in each situation. Table 3.6 shows the data pertinent to this comparison.

Table 3.6: Feedback gains reached for the damped and undamped microphones

	Undamped		Damped	
	K_p	$K_d(s)$	K_p	$K_d(s)$
Increase K_p first	4	0.0011	62	0.0001
Increase K_d first	1	0.0013	1	0.0017
IncreaseK_p and K_d together	10	0.0008	13	.0014

As seen from the table, the controller gains can be increased to a higher level before reaching instability for the damped microphone. This gives another indication of the increased operational range through the addition of membrane damping.

A third method of comparison for the damped and undamped microphones is to demonstrate the amount of control possible of the phase response for each case. This measure is particularly beneficial to beamforming array applications where being able to match the time delays for several sensors is very important. To avoid signal distortion, the microphone phase response corresponding to this time delay, τ, should vary linearly with frequency; sensors with $\zeta = 0.6$ to 0.7 have phases which are nearly straight for the widest frequency range. Assuming, however, that the linear range is wide enough for the chosen application regardless of the damping ratio, being able to manipulate τ using the feedback over a wide range of values is ideal.

When K_p is increased, the damping is decreased and the phase response slope at zero frequency decreases, yielding a smaller τ. Conversely, when K_d is increased, the damping is increased and the phase slope increases, yielding a larger τ. Figure 3.10 shows the open-loop and the closed-loop phase response for when either K_p or K_d are taken to their exteme values just before instability is reached for the undamped microphone. Figure 3.11 shows similar results for the damped microphone.

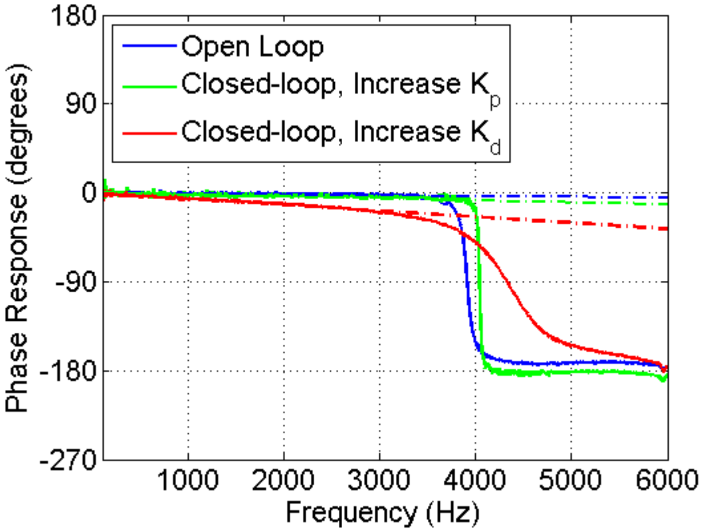

Figure 3.10: Phase delay comparison for the undamped microphone. Broken lines represent the models for the linear portions of the phase traces.

To calculate τ, the value of the phase at 1000Hz was retrieved from the data. Using this value and an assumed value of zero degrees at zero frequency, a line connecting the two points to model the linear portion of the phase could be determined. The linear range extends further than 1000Hz for many cases, but fitting over a smaller range ensured that no

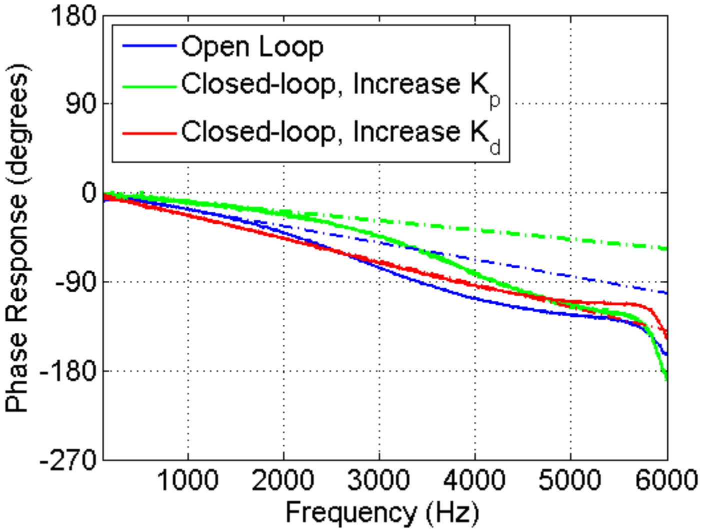

Figure 3.11: Phase delay comparison for the damped microphone. Broken lines represent the models for the linear portions of the phase traces.

nonlinear phase behavior would be influencing the calculation of τ. The τ values range from 0.8591ms (open-loop) to 6.0678ms (increase K_d) for the undamped microphone and from 9.4347ms (increase K_p) to 23.3166ms (increase K_d) for the damped microphone. The range of phase stability is extended by over 250%. The delay has a 13.9ms range for the damped microphone, an improvement over the 5.2ms range for the undamped baseline microphone design.

Chapter 4

Area-Averaging Optical Displacement Sensor to Extend Operational Range

In addition to the damping back-plates described in Chapter 3, another method for improving the operational range of the microphone is the employment of an optical sensor that averages the membrane displacement over an area larger than that of the ‘point’ sensor used previously. This is expected to decrease the observability of higher-order membrane resonance modes relative to the fundamental resonance mode (as rationalized in section 4.1) and thus increase the gain margin in closed-loop operation leading to enhanced stability.

4.1 Modeling of a Displacement-Averaging Optical Sensor

As described in Chapter 2, the membrane dynamics can be modeled with the linear wave equation. Because membrane deflection is measured at the center of the membrane, only the axi-symmetric modes of vibration are detected by the optical sensor. The non-axisymmetric resonances have zero deflection at $r = 0$. Theoretical analysis was employed in [3] to assess the expected attenuation of higher-order axisymmetric membrane resonances (which are believed to lead to instability, and hence reduced operational range, of the microphone in operation) through the measurement of an area-averaged displacement. The axisymmetric modes for a circular membrane clamped at its edges take the shape of Bessel functions of the zeroth order [9], as depicted in Figure 4.1 for the first four modes, where r is the radial coordinate in the undeflected membrane plane, z is the radial mode shape of the membrane deflection, z_C is the deflection at the membrane's center (i.e. at $r = 0$), and a is the radius of the membrane.

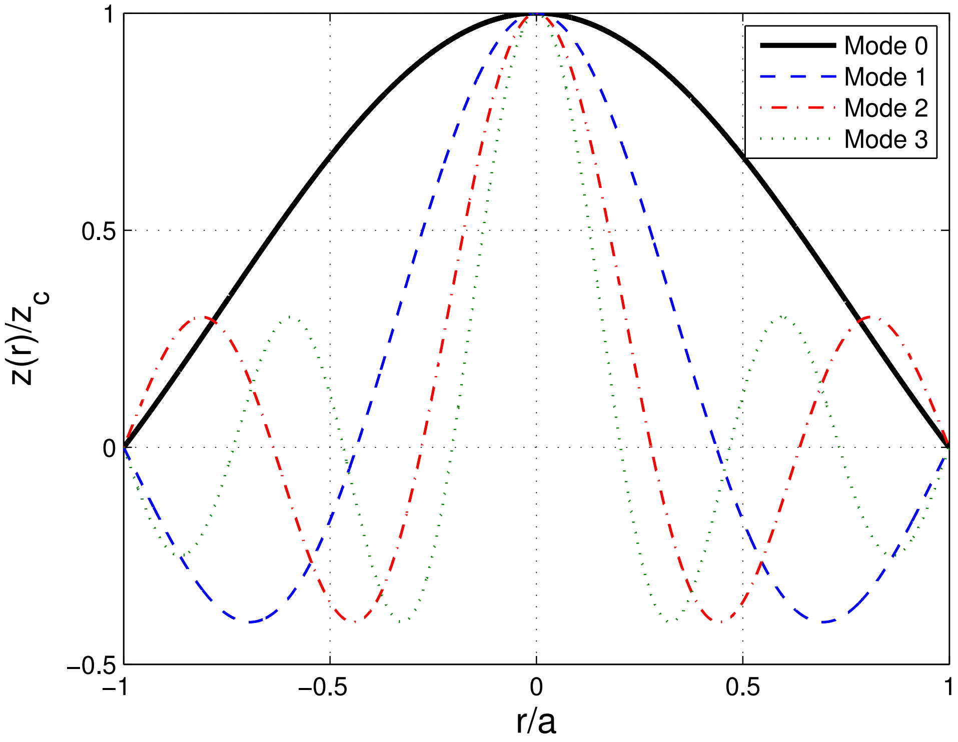

Figure 4.1: The first four axisymmetric deflection modes of a circular membrane (figure taken from [3])

Referring to Figure 4.1, it is evident that the membrane deflection associated with resonances other than the fundamental mode have both positive and negative components which, when averaged over an area, will at least partially cancel out without substantially affecting the sensed displacement of the first resonance (which is completely in phase over the averaging area). This can be demonstrated quantitatively by calculating the displacement obtained from a sensor that responds to the average displacement over an area of radius a_S centered on $r = 0$. The plot in Figure 4.2 displays the magnitude of the resulting average displacement (z_{avg}) normalized by the membrane's center displacement, plotted against the probe radius divided by the membrane's radius. It is predicted that using an optical sensor with a radius that is around 69% that of the microphone membrane would result in a significant increase in closed-loop gain margin. This is because for this ratio, the first-order mode completely cancels and the second and third resonances have minimal effect. Meanwhile, the mode of interest, the zeroth resonance, still has significant average displacement at this sensor-to-membrane radius ratio.

For this research, the area-averaging sensor utilized is lever sensor Philtec model D169 with a fiberoptic diameter of 4.29mm. This is compared to utilizing a point sensor for previous results, Philtec model D20, with a tip diameter of 0.51mm. The transfer function for the area-averaged sensor with sensitivity 35500V/m and a 20,000Hz cut-off frequency is the following:

$$G_{o,area}(s) = \frac{35500}{\frac{s}{125600} + 1} \tag{4.1}$$

The ratio of the radius of the Philtec D169 area-averaging sensor to that of the membrane is 0.34 and is indicated in Figure 4.2 with a bold black arrow along the horizontal axis.

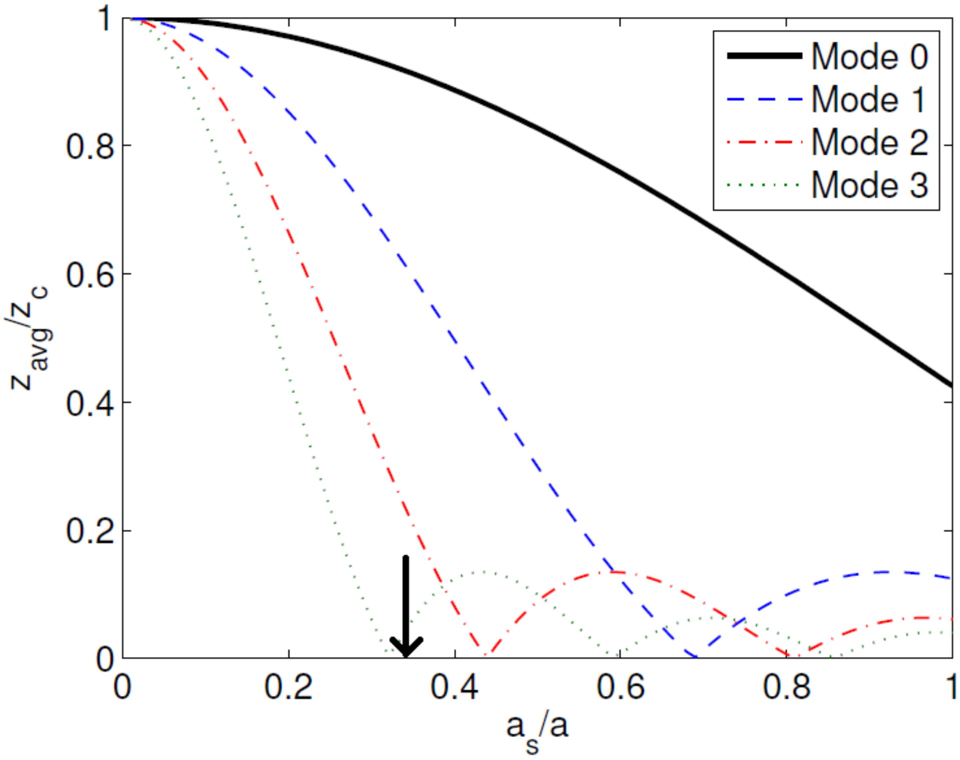

Figure 4.2: Relative average displacement of the membrane as a function of the sensor probe radius, with the lever sensor-to-membrane diameter of the prototype marked with an arrow (figure taken from [3])

Looking at Figure 4.2, the expected effect from using the D169 sensor is a relative decrease in the measured strengths of the higher-order frequencies; the design is expected to be most effective in damping mode 3. It was not possible to build a prototype with the "optimal" sensor to membrane radius ratio because on one hand, there was limited availability of optical lever sensor sizes; and also, in trying to construct smaller microphone sensors, there was difficulty in actuating the PVDF effectively.

4.2 Characterization Results of the Feedback-Controlled Microphone with Area-Averaged Sensing

4.2.1 Open-Loop Characterization

Figure 4.3 compares the open-loop microphone calibration results using the point and the area-averaged optical displacement sensors. The resonances are all sharper when measured by the point optical sensor. The fundamental resonance frequency peak is shifted slightly, perhaps due to changing membrane tension over time. The same microphone and membrane was used for both experiments, but over a month's time elapsed between recording each data set. It is significant to note that the third axisymmetric mode is damped the most, as expected based on the discussion of Figure 4.2. Comparison between the open-loop characterization results for the microphone with the area-averaging sensor and the model predictions are shown in Figure 4.4. The membrane parameters estimated from these results are listed in Table 4.1.

Table 4.1: Membrane parameters estimated from open-loop calibration of the microphone with the area-averaged displacement sensor

Parameter	**Symbol**	**Value**	**Unit**
Mass	M	0.0493	kg/m^2
Damping	C_0	91.195	$Pa \cdot s/m$
Stiffness	K_0	$24.24 \cdot 10^6$	Pa/m
Damping Ratio	ζ_0	0.0417	
Natural Frequency	f_0	3.53	kHz

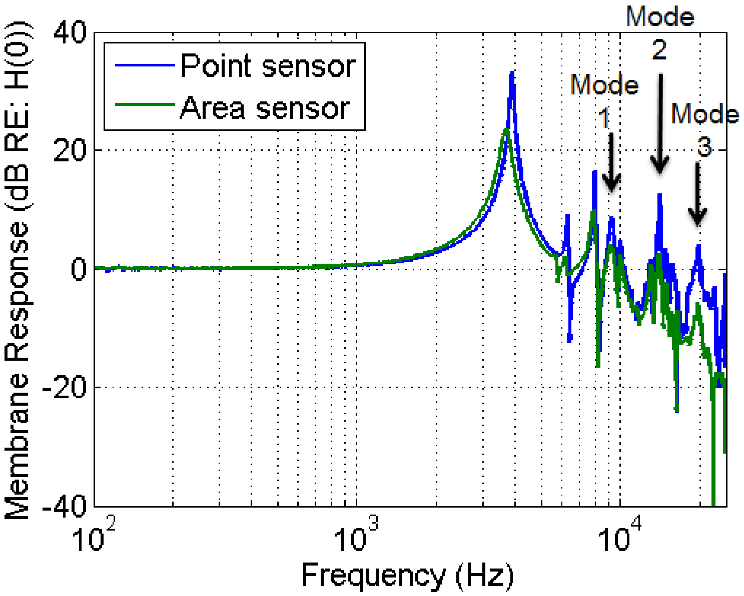

Figure 4.3: Comparison of the magnitude frequency response for the microphone with point and area-averaging displacement sensors. The first three axisymmetric modes are identified based on circular membrane vibration theory: $2.3f_r$ (9150 Hz), $3.6f_r$ (14300 Hz), and $4.9f_r$ (19500 Hz) for modes 1 to 3 respectively, based on $f_r = 3980$ Hz for the microphone with the point sensor

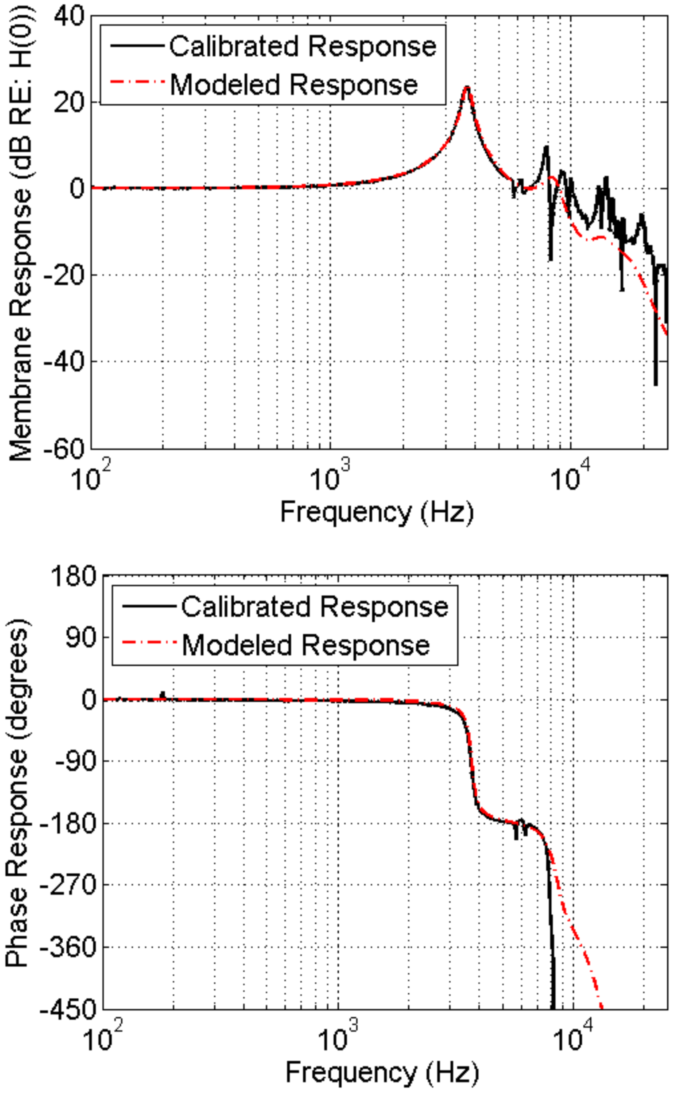

Figure 4.4: Open-loop characterization for the undamped microphone with area-averaging displacement sensor; magnitude (top); phase (bottom)

4.2.2 Feedback-Controlled Microphone Calibration Results

Figures 4.5–4.7 show the closed-loop responses for the microphone with the area-averaging sensor. Similar to closed-loop testing in previous chapters, three different methods of increasing the controller gains are implemented. In Figure 4.5, initially, the proportional gain K_p is increased until the microphone becomes unstable. This is followed by reducing K_p slightly to bring the microphone within the stability limits then increasing the derivative gain K_d to the highest possible value for stable operation. Figure 4.6 follows the same steps but in opposite order, so K_d is increased first. Finally, Figure 4.7 shows the closed-loop response when the gains K_p and K_d are increased together incrementally until just before instability is reached.

4.3 Evaluation of the Extension of the Operational Range of the Feedback-Controlled Microphone with Area-Averaging Sensing

As with the damped microphone feedback-controlled results, several methods of comparison of operational range are utilized. The first method is to measure the increase in natural frequency of the membrane. The method described in section 2.3.2 is used to determine the natural frequency and damping ratio from the data plotted in Figures 4.4–4.7 because they all have a clear fundamental resonance peak. The damping ratio and natural frequency values are summarized in Table 4.2.

Table 4.2: Natural frequencies and damping ratios for the undamped microphone with the area-averaging sensor in open- and closed-loop operation

	Open Loop	Closed Loop		
		Increase K_p first	Increase K_d first	Increase together
Natural frequency f_n (Hz)	3530	3773	4936	4603
Damping ratio ζ	0.0410	0.0122	0.0691	0.0108

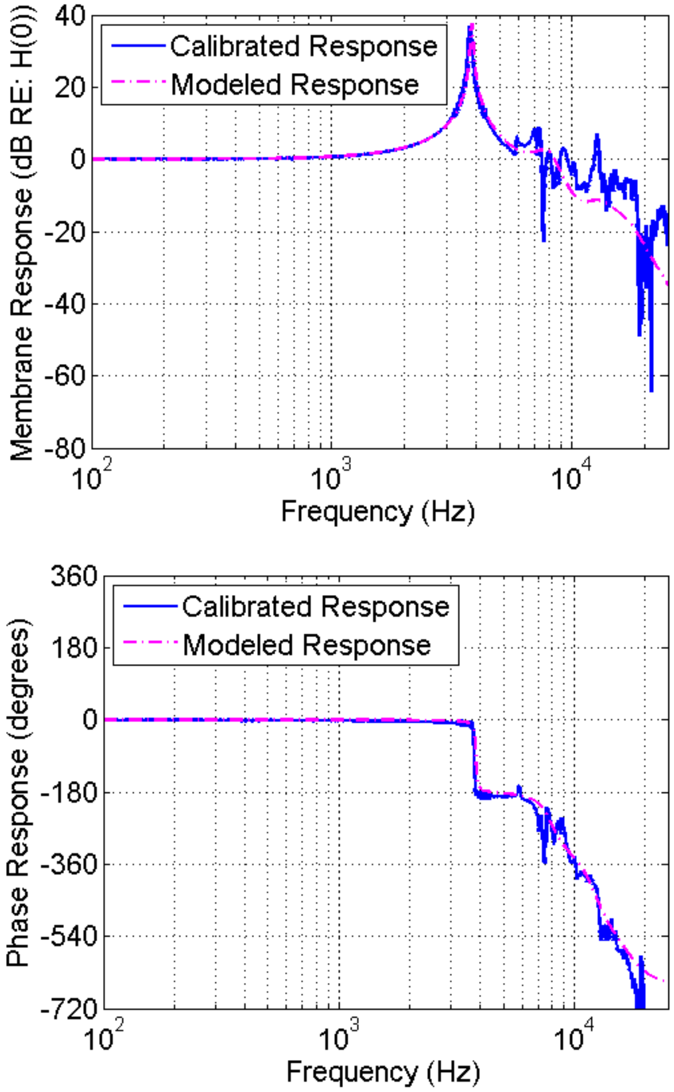

Figure 4.5: Closed-loop characterization for the undamped microphone with area-averaging displacement sensor increasing K_p first; magnitude (top); phase (bottom)

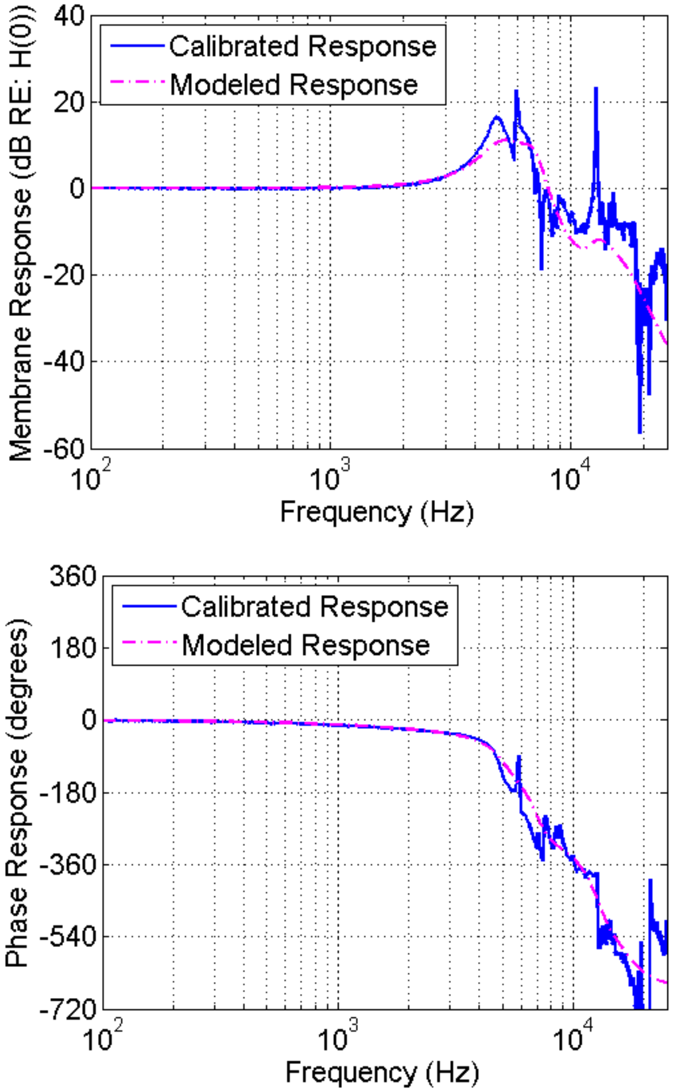

Figure 4.6: Closed-loop characterization for the undamped microphone with area-averaging displacement sensor increasing K_d first; magnitude (top); phase (bottom)

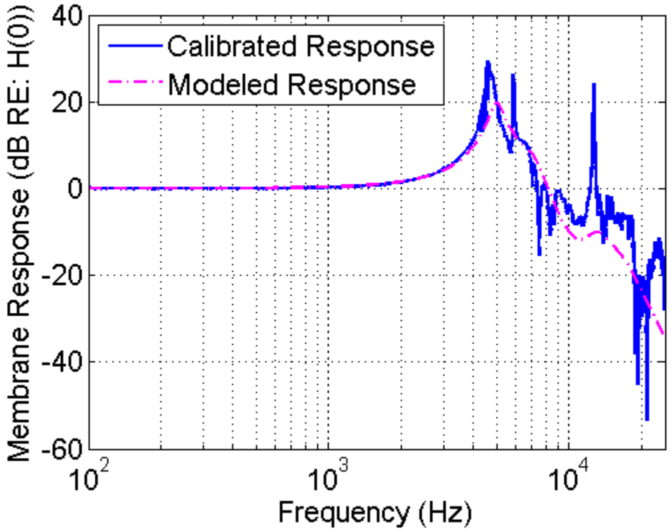

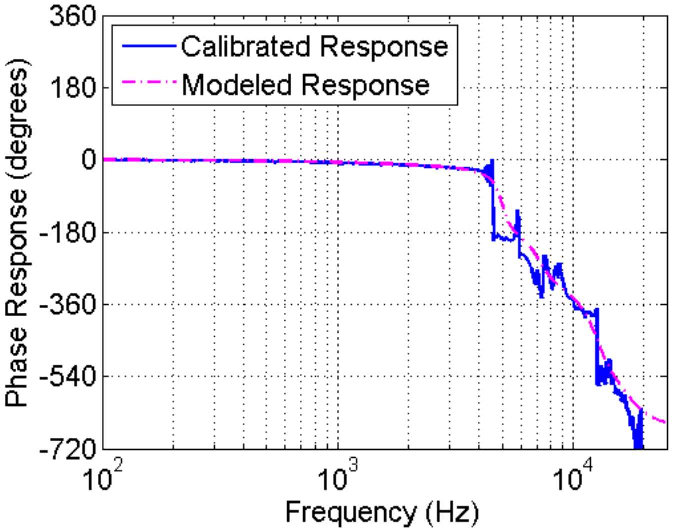

Figure 4.7: Closed-loop characterization for the undamped microphone with area-averaging displacement sensor increasing K_p and K_d simultaneously; magnitude (top); phase (bottom)

As with the point optical sensor, the closed-loop method of increasing K_d first has the highest natural frequency increase, an increase of 39.8%. This is not as high of an increase as for the damped microphone in chapter 3 (51.0%), but an improvement over the undamped microphone with the point optical sensor (16.9%). The feedback gains reached for the microphone with the area-averaging optical sensor are summarized in Table 4.3. The gains listed in Table 4.3 are higher than those listed in Table 3.6 for the undamped microphone with the point sensor. All together, the results show that in fact the use of an area-averaging sensor does increase the gain margin relative to the employment of the single-point sensor. However, for the specific configuration of damping and area-averaged sensing used here, the former is more effective in enhancing the operational range relative to the latter.

Table 4.3: Feedback gains reached for the microphone with the area-averaging optical sensor

	K_p	$K_d(s)$
Increase K_p first	16	0.0001
Increase K_d first	1	0.003
IncreaseK_p and K_d together	23	0.0022

The amount of phase control was also explored for the microphone with the area-averaging sensor. Figure 4.8 shows the open-loop and the closed-loop phase response for cases where K_p or K_d are taken to their extreme values just before instability is reached.

Following a similar procedure for demonstrating phase control as used in section 3.4, the τ values range from 5.2252 ms (increase K_p) to 15.0285 ms (increase K_d) for the undamped microphone with the area-averaging sensor. This is a 9.8 ms range, an improvement of 188% over the undamped microphone with the point optical sensor. Moreover, the 9.8 ms range is 140% of the open-loop microphone time delay (7.0253 ms), demonstrating the ability to tune the phase response of different microphones in an array over a fairly substantial range.

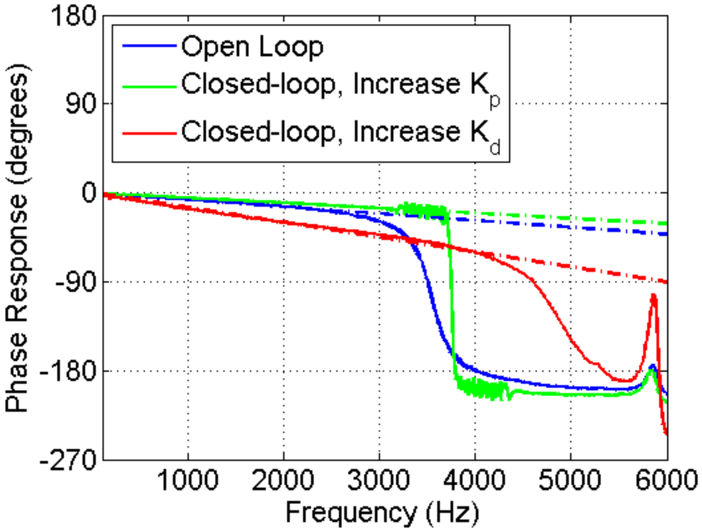

Figure 4.8: Phase delay comparison for the undamped microphone with the area-averaging optical sensor. Broken lines represent the models for the linear portions of the phase traces.

4.4 Characterization Results of the Feedback-Controlled Microphone with Area-Averaged Sensing and Damped Membrane

After implementing the damping back-plates and the area-averaging sensor individually, the next natural step is to combine the two provisions. Figure 4.9 shows the open-loop microphone calibration for this combination. The closed-loop results are given in Figures 4.10–4.12.

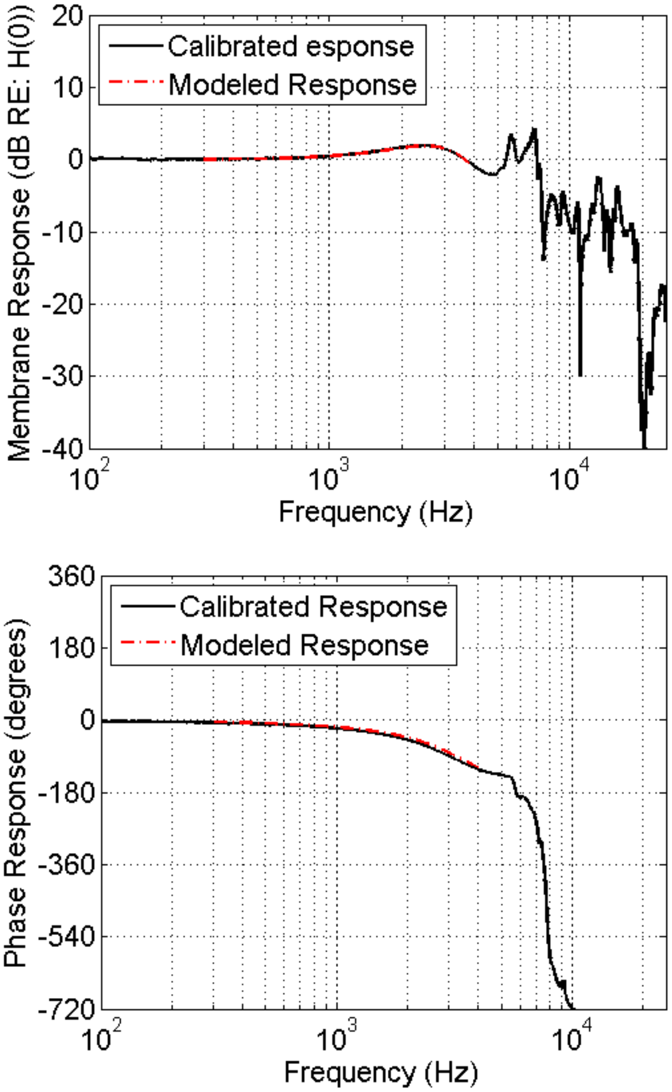

Figure 4.9: Open-loop characterization for the damped microphone with the area-averaging displacement sensor; magnitude (top); phase (bottom)

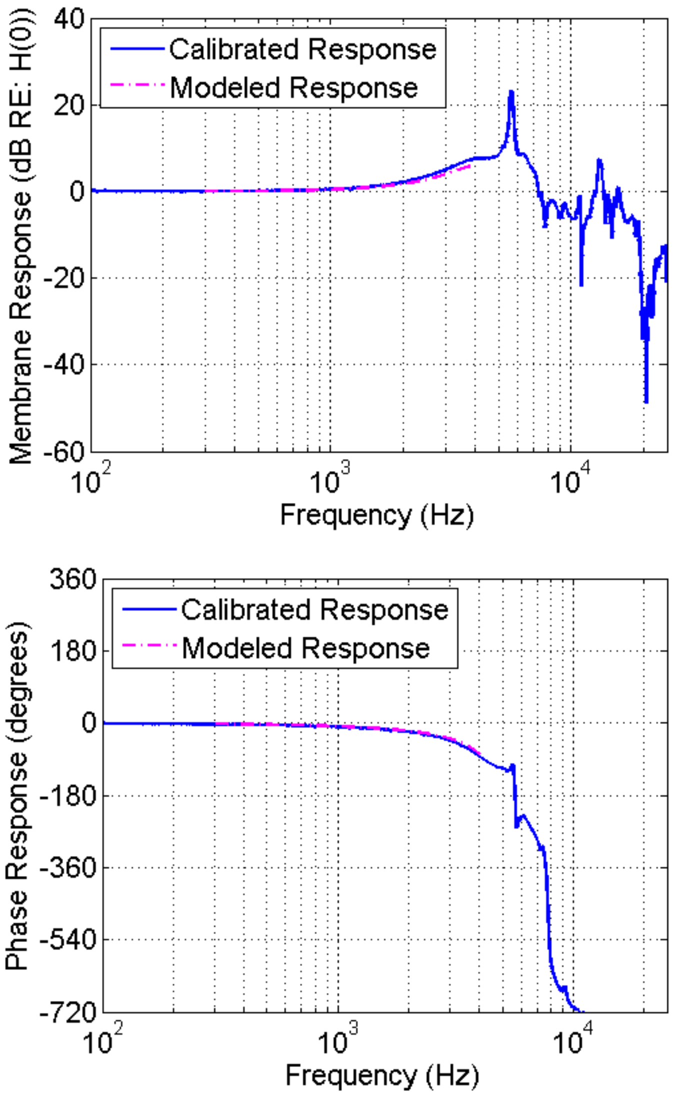

Figure 4.10: Closed-loop characterization for the damped microphone with area-averaging displacement sensor, increasing K_p first; magnitude (top); phase (bottom)

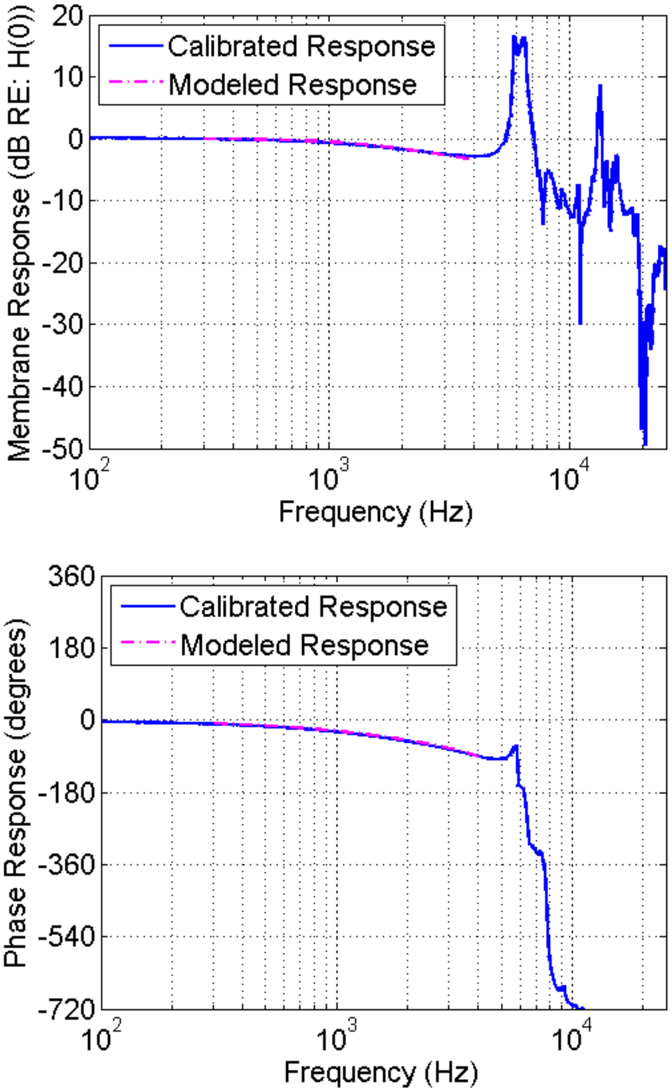

Figure 4.11: Closed-loop characterization for the damped microphone with area-averaging displacement sensor, increasing K_d first; magnitude (top); phase (bottom)

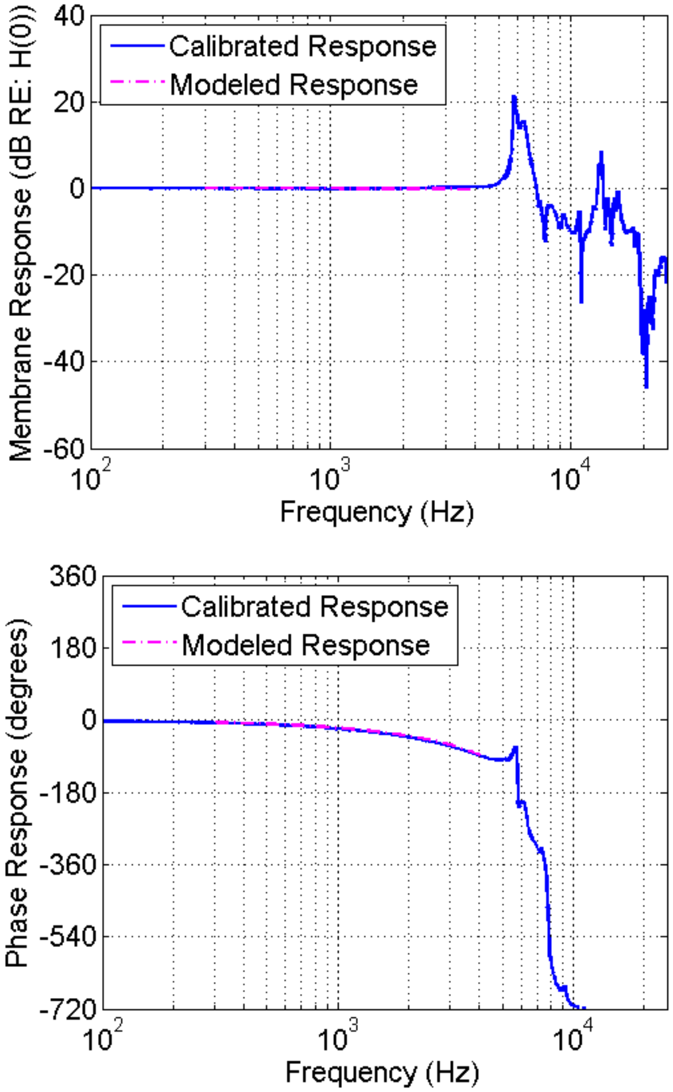

Figure 4.12: Closed-loop characterization for the damped microphone with area-averaging displacement sensor, increasing K_p and K_d simultaneously; magnitude (top); phase (bottom)

Using the method described in section 3.3.1, a best fit model was used to determine the natural frequency and damping ratio for the responses in Figures 4.9–4.12. This is summarized in Table 4.4. The closed-loop calibrations for the cases when K_d was increased first and when K_p and K_d were increased together have no values listed because the best fit method yielded imaginary numbers. This is believed to be caused by the membrane's response becoming over-damped at the first fundamental resonance. One can observe though, from the plots, that a relatively flat response is obtained for a wide range of frequencies, especially for the case when K_p and K_d are increased together.

Table 4.4: Natural frequencies and damping ratios for the damped microphone with the area-averaging sensor in open- and closed-loop operation

	Open Loop	Closed Loop		
		Increase K_p first	Increase K_d first	Increase together
Natural frequency f_n (Hz)	3315	4051	?	?
Damping ratio ζ	0.4837	0.2606	?	?

Table 4.5 lists the gains reached before operation became unstable for each situation. These are the highest gains reached for any of the microphones, an expected result when combining both methods of improving the operational range.

Table 4.5: Feedback gains reached for the damped microphone with the area-averaging optical sensor

	K_p	$K_d(s)$
Increase K_p first	93	0.0001
Increase K_d first	0.5	0.0042
IncreaseK_p and K_d together	30	0.003

As with the damped-membrane microphone and the microphone utilizing the area-averaging sensor, the phase control was examined for the microphone with both the damped membrane and the area-averaging sensor. Figure 4.13 shows the open-loop and closed-loop phase response when either K_p or K_d are taken to their extreme values just before instability is reached. Here, the τ values have their widest range, from 10.1107ms (increase K_p) to 30.2893ms (increase K_d). This 20.2ms range is a 388% improvement over the baseline design (i.e. the open-loop response of a microphone with undamped membrane and with point displacement sensor) and is the widest range of phase control for any of the microphone designs tested.

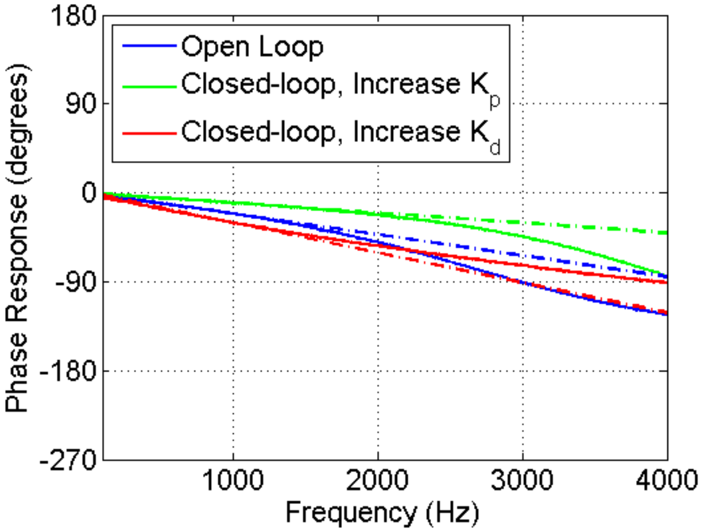

Figure 4.13: Phase delay comparison for the damped microphone with the area-averaging optical sensor. Broken lines represent the models for the linear portions of the phase traces.

Chapter 5

Summary and Recommendations

This study was undertaken with the intent to extend the operational range of a feedback-controlled microphone developed recently at MSU in [2] and [3].

Mechanical damping provisions were introduced to decrease the strength of the microphone membrane's high-order resonance peaks which limit the stability. Chapter 3 provides a description of implementing said damping provisions through the use of back-plates with small holes that were designed and fabricated in the present work using laser ablation at NASA Langley Research Center. The results demonstrated that, through several methods of quantifying the microphone's operational range, the damped response was always an improvement over the undamped response. Natural frequencies reached higher percent increases; controller gains were pushed to greater limits before instability was reached; and phase delays were capable of spanning larger ranges for the damped-membrane microphone.

Chapter 4 gives a description of the improvements in microphone operational range expected from using an area-averaging fiber-optic sensor as well as including results demonstrating those improvements. The increases in stability over the baseline design were not as dramatic as those for the damped-membrane microphone as described in Chapter 3, but there was still a measurable improvement. Also explored in Chapter 4 was the extension of operational range for the microphone employing both methods of decreasing the strength of membrane resonances (damping provisions and area-averaging optical sensor). This combination yielded the greatest improvement of all.

Figure 5.1 shows a summary plot demonstrating the relative improvement for the different microphones tested. It compares the baseline open-loop response with closed-loop responses for both damped and undamped membrane, and for both point and area-averaging optical sensor. Using the standard method of identifying bandwidth as the frequency band over which the magnitude response remains within ± 3dB (broken thick black lines in Figure 5.1), it is seen that the provisions implemented here are capable of approximately tripling the microphone's bandwidth. In comparison, in previous studies at Michigan State University, the best improvement in bandwidth was only an approximate doubling of the bandwidth.

A recommendation to further validate the research pertaining to this feedback-controlled microphone is to build an array of two or more sensors that is programmed to demonstrate the 'self-calibrating' capability. A frequency sweep can be input to each sensor and the two microphones can be electrically calibrated. Then, based on the parameters calculated from this, feedback can be used to tune the response of one sensor to match the other; again, this ability to use feedback to obtain a predicted response was demonstrated in [2] and [3].

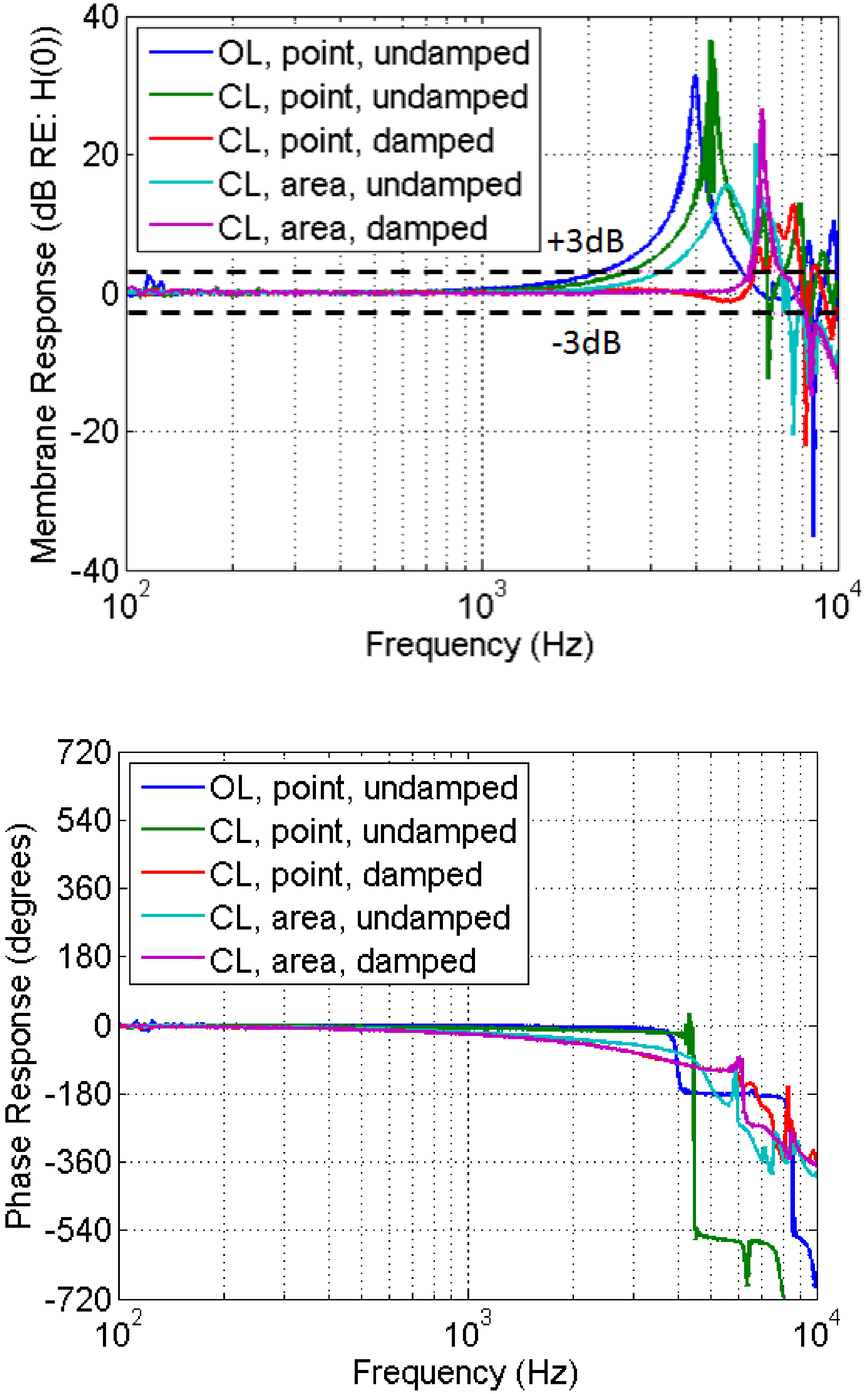

Figure 5.1: A comparison of frequency and phase response for several of the tested microphone designs; magnitude (top); phase (bottom). Broken lines on top plot represent the ± 3dB boundaries for identifying the bandwidth

Another proposal for improvement is to work with a smaller membrane diameter. This would give a larger bandwidth. Microphones with membrane diameters of three eighths inch and one quarter inch were constructed; but they were not tested because sufficient actuation of the PVDF membrane could not be achieved. The signal-to-noise ratio was too great. A recommendation is to explore the use of a higher-voltage piezo-driver.

Damping back-plates were also constructed for the smaller microphone sensor sizes, so once the PVDF actuation issue for these is resolved, the fabricated back-plates can be implemented. Relating to the damping back-plates, it was observed in Chapter 3 that the model used to determine the amount of damping achieved by using the discs was less accurate than expected. Modification to the model is necessary. A possible improvement is to include the air gap between the membrane and the back-plate, previously excluded from the model. This gap was smaller in the design employed in [2] and [3] but when the microphone capsule was redesigned to accommodate the damping back-plates, this gap became bigger.

A final recommendation is to construct a microphone with the hypothesized 'ideal' optical sensor-to-membrane diameter ratio. As discussed in Chapter 4, the suggested optimal ratio is 0.69, thought to be the ratio where the first three high-order resonance modes' magnitudes are decreased the most relative to the fundamental resonance. Further experimentation with other ratios is also recommended.

Appendix A

Hole Coordinates of Fabricated Damping Back-Plates

Table A.1: Polar coordinates of the holes in the damping back-plate with the 91-hole pattern and circular arrangement

Hole #	r (μm)	θ (deg)
1	0	0
2	1000	0
3	1000	60
4	1000	120
5	1000	180
6	1000	240
7	1000	300
8	2000	0
9	2000	30
10	2000	60
11	2000	90
12	2000	120
13	2000	150
14	2000	180
15	2000	210
16	2000	240
17	2000	270
18	2000	300
19	2000	330
20	3000	0
21	3000	20
22	3000	40
23	3000	60
24	3000	80
25	3000	100
26	3000	120
27	3000	140
28	3000	160
29	3000	180
30	3000	200
31	3000	220
32	3000	240
33	3000	260
34	3000	280
35	3000	300
36	3000	320
37	3000	340
38	4000	0
39	4000	15
40	4000	30
41	4000	45
42	4000	60
43	4000	75
44	4000	90
45	4000	105
46	4000	120
47	4000	135
48	4000	150
49	4000	165
50	4000	180
51	4000	195
52	4000	210
53	4000	225
54	4000	240
55	4000	255
56	4000	270
57	4000	285
58	4000	300
59	4000	315
60	4000	330
61	4000	345
62	5000	0
63	5000	12
64	5000	24
65	5000	36
66	5000	48
67	5000	60
68	5000	72
69	5000	84
70	5000	96
71	5000	108
72	5000	120
73	5000	132
74	5000	144
75	5000	156
76	5000	168
77	5000	180
78	5000	192
79	5000	204
80	5000	216
81	5000	228
82	5000	240
83	5000	252
84	5000	264
85	5000	276
86	5000	288
87	5000	300
88	5000	312
89	5000	324
90	5000	336
91	5000	348

Table A.2: Polar coordinates of the holes in the damping back-plate with the 121-hole pattern and circular arrangement

Hole #	r (μm)	θ (deg)
1	0	0
2	950	0
3	950	60
4	950	120
5	950	180
6	950	240
7	950	300
8	1900	0
9	1900	30
10	1900	60
11	1900	90
12	1900	120
13	1900	150
14	1900	180
15	1900	210
16	1900	240
17	1900	270
18	1900	300
19	1900	330
20	2850	0
21	2850	20
22	2850	40
23	2850	60
24	2850	80
25	2850	100
26	2850	120
27	2850	140
28	2850	160
29	2850	180
30	2850	200
31	2850	220
32	2850	240
33	2850	260
34	2850	280
35	2850	300
36	2850	320
37	2850	340
38	3800	0
39	3800	15
40	3800	30
41	3800	45
42	3800	60
43	3800	75
44	3800	90
45	3800	105
46	3800	120
47	3800	135
48	3800	150
49	3800	165
50	3800	180
51	3800	195
52	3800	210
53	3800	225
54	3800	240
55	3800	255
56	3800	270
57	3800	285
58	3800	300
59	3800	315
60	3800	330
61	3800	345
62	4750	0
63	4750	12
64	4750	24
65	4750	36
66	4750	48
67	4750	60
68	4750	72
69	4750	84
70	4750	96
71	4750	108
72	4750	120
73	4750	132
74	4750	144
75	4750	156
76	4750	168
77	4750	180
78	4750	192
79	4750	204
80	4750	216
81	4750	228
82	4750	240
83	4750	252
84	4750	264
85	4750	276
86	4750	288
87	4750	300
88	4750	312
89	4750	324
90	4750	336
91	4750	348
92	5700	0
93	5700	12
94	5700	24
95	5700	36
96	5700	48
97	5700	60
98	5700	72
99	5700	84
100	5700	96
101	5700	108
102	5700	120
103	5700	132
104	5700	144
105	5700	156
106	5700	168
107	5700	180
108	5700	192
109	5700	204
110	5700	216
111	5700	228
112	5700	240
113	5700	252
114	5700	264
115	5700	276
116	5700	288
117	5700	300
118	5700	312
119	5700	324
120	5700	336
121	5700	348

Table A.3: Cartesian coordinates of the holes in the damping back-plate with the 91-hole pattern and hexagonal arrangement

Hole #	x (μm)	y (μm)
1	0	0
2	1000	0
3	2000	0
4	3000	0
5	4000	0
6	5000	0
7	-1000	0
8	-2000	0
9	-3000	0
10	-4000	0
11	-5000	0
12	500	866
13	1500	866
14	2500	866
15	3500	866
16	4500	866
17	-500	866
18	-1500	866
19	-2500	866
20	-3500	866
21	-4500	866
22	500	-866
23	1500	-866
24	2500	-866
25	3500	-866
26	4500	-866
27	-500	-866
28	-1500	-866
29	-2500	-866
30	-3500	-866
31	-4500	-866
32	0	1732
33	1000	1732
34	2000	1732
35	3000	1732
36	4000	1732
37	-1000	1732
38	-2000	1732
39	-3000	1732
40	-4000	1732
41	0	-1732
42	1000	-1732
43	2000	-1732
44	3000	-1732
45	4000	-1732
46	-1000	-1732
47	-2000	-1732
48	-3000	-1732
49	-4000	-1732
50	500	2598
51	1500	2598
52	2500	2598
53	3500	2598
54	-500	2598
55	-1500	2598
56	-2500	2598
57	-3500	2598
58	500	-2598
59	1500	-2598
60	2500	-2598
61	3500	-2598
62	-500	-2598
63	-1500	-2598
64	-2500	-2598
65	-3500	-2598
66	0	3464
67	1000	3464
68	2000	3464
69	3000	3464
70	-1000	3464
71	-2000	3464
72	-3000	3464
73	0	-3464
74	1000	-3464
75	2000	-3464
76	3000	-3464
77	-1000	-3464
78	-2000	-3464
79	-3000	-3464
80	500	4330
81	1500	4330
82	2500	4330
83	-500	4330
84	-1500	4330
85	-2500	4330
86	500	-4330
87	1500	-4330
88	2500	-4330
89	-500	-4330
90	-1500	-4330
91	-2400	-4330

BIBLIOGRAPHY

BIBLIOGRAPHY

[1] Humphreys, W.M., T.F. Brooks, W.W. Hunter, and K.R. Meadows, *Design and Use of Microphone Directional Arrays for Aeroacoustic Measurements*, 36th Aerospace Sciences Meeting & Exhibit, AIAA Paper number 98-0471, Reno, NV, Jan 12-15 (1998)

[2] Radcliffe, E., A.M. Naguib, and W.M. Humphreys, Jr., *A Novel Design of a Feedback-Controlled Optical Microphone for Aeroacoustics Research*, Meas. Sci Technol, Vol. 21, 105208, 2010

[3] Radcliffe, E., *Development and Characterization of an Optical Feedback Controlled Microphone for Aeroacoustics Research*, MS Thesis, Michigan State University, East Lansing, 2010. Print.

[4] Tamura, M., T. Yamaguchi, T. Oyaba, T. Yoshimi, *Electroacoustic Transducers with Piezoelectric High Polymer Films*, 49th Convention of the Audio Engineering Society, New York, NY, Sept. 10 (1974)

[5] Lerch, R., *Electroacoustic transducers using piezoelectric polyvinylideneflouride films*, J. Acoust. Soc. Am. **66** 4, 952-954 (1979)

[6] Howarth, T.R., J.F. Tressler, J.A. Bucaro, *Piezoelectric Acoustic Actuator*, U.S. Patent No. 6,717,337, Apr. 6, (2004)

[7] Zuckerwar, A.J., *Principles of Operation of Condenser Microphones*, AIP handbook of condenser microphones, theory calibration and measurements, 45-57, AIP Press, New York (1994)

[8] Kinsler, L., A.R. Frey, A.B. Coppens, J.V. Sanders, *Fundamentals of Acoustics* –3rd ed. John Wiley & Son, New York (1982)

[9] Meirovitch, L., *Analytical Methods in Vibrations*, MacMillan, New York (1967)